

CHAPTER 1

LOCALIZED EXCITATIONS IN JOSEPHSON ARRAYS. PART I: THEORY AND MODELING

Juan J. Mazo

*Departamento de Física de la Materia Condensada
Universidad de Zaragoza, 50009 Zaragoza, Spain*

*Instituto de Ciencia de Materiales de Aragón (ICMA),
C.S.I.C. – Universidad de Zaragoza, 50009 Zaragoza, Spain*

*Instituto de Biocomputación y Física de Sistemas Complejos (BIFI),
Universidad de Zaragoza, 50009 Zaragoza, Spain*

E-mail: juanjo@unizar.es

Josephson-junction arrays are excellent experimental systems for the study of nonlinear phenomena in general and nonlinear localised excitations in particular. This chapter is an introduction to the physics of vortices, kinks and breathers in Josephson arrays. Special emphasis is placed in the description of discrete breather solutions.

1. Introduction

The concept of coherent structures or coherent excitations has important consequences when applied to condensed matter systems. Spatially or temporally coherent structures appear in many nonlinear extended systems. Such structures usually can be characterized by marked particle-like properties. In the past few years, these notions have become fundamental for understanding many problems and their implications extend over different fields of the physics of continuous and discrete systems.¹

Josephson-junction (JJ) arrays are a very well example of an experimental system where such type of structures appear. Examples are vortices, kinks and discrete breathers. This article is an introduction to the physics of these excitations with special attention given to the study of discrete breather (DB) solutions.

In section 2, we will introduce the main aspects of the physics of single

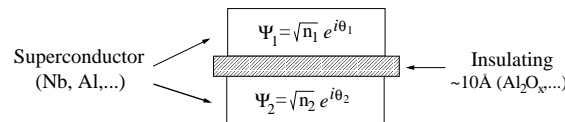


Fig. 1. Schematic of a Josephson tunnel junction

JJs. In section 3 we will present a method to model Josephson arrays. This section is focused in the introduction of the equations that we will use to study the different localized excitation in the arrays. In section 4 we will review some aspects of the work about vortices in two-dimensional JJ arrays and kinks in one-dimensional parallel arrays. Section 5 is the main section of this report. There, we will study discrete breathers in Josephson arrays. We focus on theoretical and numerical results since most of the experimental details are included in the chapter ?? of this book written by Alexey Ustinov.

2. The single Josephson junction

2.1. Josephson effect

In his work of 1962² Brian Josephson studied the tunnel of Cooper pairs between superconducting metals and predicted the celebrated Josephson effect. Since then, hundreds of works have been done which study the behavior of single junctions, JJ arrays, and other more complex devices with Josephson elements. Some books and references on Josephson effect in weakly coupled superconductors are Refs. 3-7

It is important to say however, that although mainly used in the context of superconductivity, the physics behind the name of “Josephson effect” applies to other weakly coupled macroscopic quantum systems.⁸ Examples are the studies of the Josephson effect in weakly coupled superfluids (see Ref. 9 for instance) and the recent interest on Josephson effect in weakly coupled Bose-Einstein condensates (see Ref. 10 for instance).

2.2. Superconducting tunnel junctions

A Josephson tunnel junction is a solid state physics device which consist of two superconducting electrodes (usually Niobium or Aluminum) separated by a thin insulating barrier (usually an Aluminum oxide), see Fig. 1.

The physics of the junction is controlled by the value of the gauge invariant phase difference between the superconducting electrodes $\varphi =$

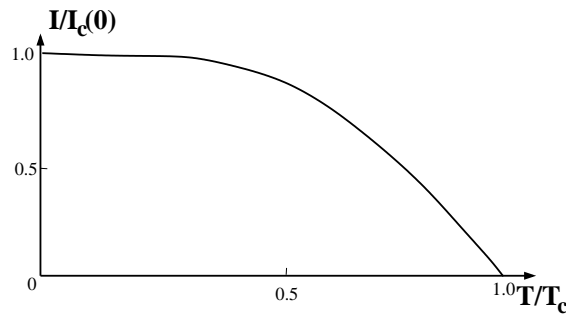


Fig. 2. Temperature dependence of the junction critical current.

$\theta_1 - \theta_2 - \frac{2e}{\hbar} \int_1^2 \vec{A}(\vec{r}, t) d\vec{l}$, with θ_i the phase of the macroscopic wave function in electrode i ($\Psi_i = \sqrt{|\Psi_i|} e^{i\theta_i}$) and \vec{A} the vector potential.

The basic equations for the Josephson effect are

$$I_s = I_c \sin \varphi \quad (1)$$

and

$$V = \frac{\hbar}{2e} \frac{d\varphi}{dt}. \quad (2)$$

They establish – *DC Josephson effect* – that at zero voltage (then φ is constant) it is possible to have a dc current across the junction. The maximum possible value of this current is I_c , the junction critical current. However – *AC Josephson effect* – in the presence of a constant voltage the junction responds with an ac current of frequency $2eV/\hbar$ (483.6 GHz/mV).

We want to mention here that the $\hbar/2e$ quotient can be also written in terms of the flux quantum unit $\Phi_0 = h/2e$. Thus $\hbar/2e = \Phi_0/2\pi$.

The potential energy associated with the supercurrent across the junction is given by

$$U_J = -E_J \cos \varphi, \quad (3)$$

with $E_J = \hbar I_c/2e$. A first requirement to observe Josephson effect is that the Josephson energy exceeds the thermal energy $E_J \gg k_B T$ ($I_c \gg 2ek_B T/\hbar$).

The junction critical current I_c has a strong temperature dependence (Fig. 2) which is usually approached by the Ambegaokar-Baratoff equation¹¹

$$I_c R_n = \frac{\pi \Delta}{2e} \tanh(\Delta/2k_B T). \quad (4)$$

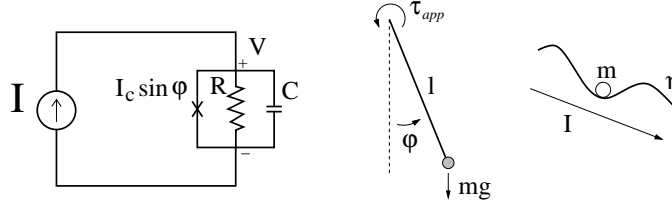


Fig. 3. RCSJ circuit model of the junction and two mechanical analogs: the forced and damped pendulum and the particle in the tilted washboard potential.

R_n is the normal state resistance of the junction and $\Delta(T)$ the superconducting gap energy. At $T=0$ we get $I_c R_n = \pi \Delta(0) / 2e$ with $\Delta(0) = 1.764 k_B T_c$ and for $T \rightarrow T_c$, $I_c R_n \simeq (2.34 \pi k_B / e)(T_c - T)$.

To study the current-voltage (IV) characteristics of the junction we use the so called RCSJ (resistively and capacitively shunted junction) model^{12,13} (see Fig. 3). In this model the total current through the junction is the sum of three contributions: the Josephson supercurrent, a resistive normal current (tunneling of normal carriers from one electrode to the other) and a capacitive channel (associated with the junction capacitance); $I = I_J + I_R + I_C$ with $I_J = I_c \sin \varphi$, $I_R = V/R$ and $I_C = C dV/dt$. Then

$$I = C \dot{V} + \frac{1}{R} V + I_c \sin \varphi. \quad (5)$$

If we apply the second Josephson relation [$V = (\Phi_0 / 2\pi)(d\varphi/dt)$] and normalize current with respect to the junction critical current, $i = I/I_c$, time with respect to the Josephson plasma frequency $\omega_p = \sqrt{2\pi I_c / \Phi_0 C}$ and introduce the damping parameter $\Gamma = \sqrt{\Phi_0 / 2\pi I_c C R^2}$ ^a, we obtain

$$i = \mathcal{N}(\varphi) = \ddot{\varphi} + \Gamma \dot{\varphi} + \sin \varphi. \quad (6)$$

This is the normalized equation for the dynamics of a single junction biased by an external current. This equation is identical to the equation for a forced and damped pendulum in a gravitational field or a particle in a tilted washboard potential $U(\varphi) = -E_J \cos \varphi - (\hbar I / 2e) \varphi$ [mass $m = (\hbar / 2e)^2 C$ and damping $\gamma = (\hbar / 2e)^2 (1/R)$], see Fig. 3. Both are simple mechanical analogs for the junction and illustrate that JJ devices are ideal experimental systems to probe basic nonlinear science results.

Figure 4 shows numerically computed IV curves of a junction at two different values of the damping. At large damping (figure at $\Gamma=5$) the voltage is

^aThe damping can be also defined in terms of the so-called quality factor $Q = 1/\Gamma$ or the Stewart-McCumber parameter $\beta_c = 1/\sqrt{\Gamma} = 2\pi I_c C R^2 / \Phi_0$

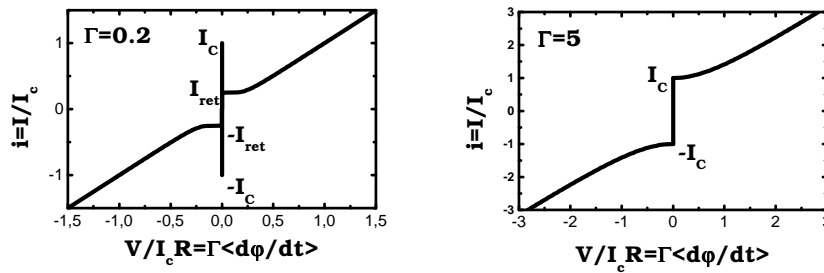


Fig. 4. IV curve for a JJ with a linear resistor biased by a dc current (Eq. 6). At $\Gamma = 0.2$ two solutions coexist for currents between the critical and the retrapping currents (underdamped case). At $\Gamma = 5.0$ (overdamped case) the voltage is a unique function of the current.

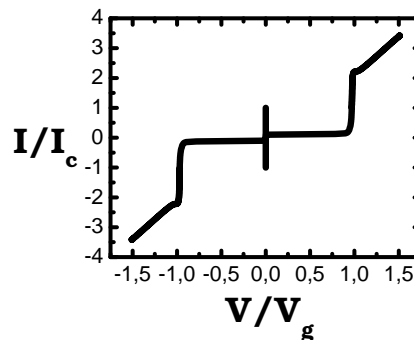


Fig. 5. Experimental IV curve of a single junction. The resistance of the junction below the gap voltage (subgap resistance) clearly differs from the resistance above the gap voltage (normal resistance).

a unique function of the current. It increases continuously from zero as soon as $I > I_c$ and approaches the ohmic relation ($I = V/R$, or $i = \Gamma \langle d\varphi/d\tau \rangle$ in normalized units) at high currents. At smaller values of the damping however the IV curve is hysteretic (see figure at $\Gamma=0.2$). Increasing the current, at $I = I_c$ the junction switches from the zero voltage state to the resistive branch $I = V/R$. If we now decrease the current, the voltage decreases continuously to zero at $I = I_{\text{ret}}$. For small enough values of Γ , $I_{\text{ret}}/I_c \simeq 4\Gamma/\pi$.

Figure 5 shows the experimental IV curve of a Niobium-Aluminum Oxide-Niobium tunnel junction. We observe that at I_c the voltage switches from 0 to the gap voltage $V_g = 2\Delta(T)/e$ ($V_g/I_c R_n = 4/\pi$ at small T). This

voltage corresponds to the energy for breaking Cooper pairs. At larger values of the current the voltage increases and follows the ohmic dependence with a resistance given by the normal state resistance R_n . Decreasing the current the voltage decreases back to the gap voltage and then to zero at a small value of the current. This nonlinear dependence shows the existence of different dissipation regimes for voltages above and below the gap voltage. Transport above the gap voltage is governed by normal state electrons meanwhile transport below the gap is usually governed by the number of quasi-particles.

A simple approach to describe such behavior is to use the RCSJ model with a nonlinear resistance $R(V)$ such that $R=R_n$ if $V>V_g$ and $R=R_{sg}(T)$ if $V<V_g$. The sub-gap resistance usually shows a marked temperature dependence governed by $R_{sg}(T) \simeq R_n e^{\Delta/k_B T}$.

An expression for the quasi-particle tunneling current valid for $k_B T \ll \Delta$ and $V < V_g$ is given by¹⁴

$$I_{qp} = \frac{2}{eR_n} e^{-\Delta/k_B T} \left(\frac{2\Delta}{eV + 2\Delta} \right)^{1/2} (eV + \Delta) \sinh \left(\frac{eV}{2k_B T} \right) K_0 \left(\frac{eV}{2k_B T} \right). \quad (7)$$

For some investigations and applications it is convenient to shunt the junction by a small resistance. In this case the equivalent resistance of the junction is small and voltage independent. It gives a large value of Γ and the overdamped limit of the RCSJ model is appropriate.

In other cases, especially when dealing with small junctions, in order to describe the behavior of the system it is essential to consider also the impedance of the external circuit.

Thermal fluctuations can be included in the model by the addition of a noise current source $\tilde{I}(t)$ with $\langle \tilde{I}(t) \rangle = 0$ and $\langle \tilde{I}(t) \tilde{I}(t') \rangle = (2k_B T/R) \delta(t - t')$. The total current, in normalized units, is

$$i = \mathcal{N}(\varphi) = \ddot{\varphi} + \Gamma \dot{\varphi} + \sin \varphi + \tilde{i} \quad (8)$$

with $\langle \tilde{i}(\tau) \rangle = 0$ and $\langle \tilde{i}(\tau) \tilde{i}(\tau') \rangle = (2\Gamma k_B T/E_J) \delta(\tau - \tau')$.

In the presence of temperature, close to I_c the junction can escape from the zero voltage state via thermal fluctuations, and close to I_{ret} can retrap to the zero voltage state (Fig. 6). Such process can be analyzed in terms of the escape of a single particle from a potential well. The escape rate Γ_{esc} in the classical regimen can be approached to

$$\Gamma_{\text{esc}} = a_t \frac{\omega}{2\pi} \exp \left(-\frac{\Delta U}{k_B T} \right), \quad (9)$$

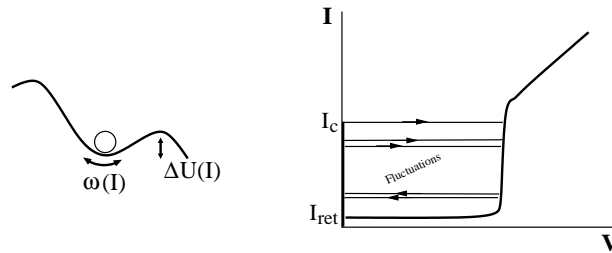


Fig. 6. The escape from the superconducting state of a junction in the presence of thermal fluctuations is a problem analogous to the escape of a particle from a well in a tilted cosine potential.

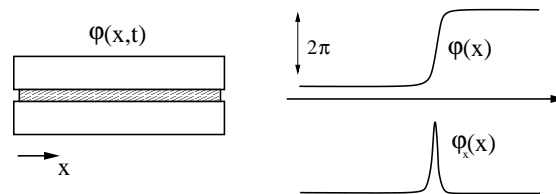


Fig. 7. Schematic of a long JJ (left) and phase and phase derivative for a soliton in the junction (right).

where a_t is a prefactor which depends on the value of the damping.^{15,16}

2.3. Long Josephson junctions

A long Josephson junction (Fig. 7) is a junction which has one dimension (say x) long with respect to the so called Josephson penetration depth.⁴ Then the phase difference is also a function of the spatial coordinate: $\varphi(x, t)$.

The electrodynamics of the junction is described by a nonlinear partial differential equation that, neglecting dissipative effects, can be written as

$$\varphi_{xx} - \varphi_{tt} = \sin \varphi. \quad (10)$$

This is the sine-Gordon equation, which has coherent localized particle-like solutions or soliton solutions. $\varphi(x)$ can be thought of as the phase difference or the normalized magnetic flux. Then a soliton in the junction corresponds to a solution for which the phase difference goes from 0 to 2π ; or the flux from 0 to Φ_0 ; that is, a fluxon of magnetic field.

When losses and bias are included the dynamics of the fluxon is described by the perturbed sine-Gordon equation

$$\varphi_{xx} - \varphi_{tt} - \sin \varphi = \alpha \varphi_t - \beta \varphi_{xxt} - \gamma. \quad (11)$$

In this lecture we are not going to deal with long JJ. For a good recent review on the subject see¹⁷ and references within.

2.4. Quantum effects in Josephson junctions

In despite of its quantum mechanical origin, we have considered above that φ behaves as a classical function. This is right for large enough junctions where quantum effects can be neglected and a classical description of the junction observables is correct.

In a Josephson junction the phase difference across the junction and the charge on the junction electrode behave as quantum-mechanically conjugate variables. The Hamiltonian for the junction can be written as the addition of Josephson and charging energy

$$H = -E_J \cos \varphi + \frac{Q^2}{2C} \quad (12)$$

where $Q \sim d\varphi/dt$.

To study the dynamics of the junction we will follow canonical quantization rules and treat φ and Q as operators which satisfy the usual commutation rule $[\varphi, Q] = i2e$. Then, in phase representation, we substitute $Q/2e = N$ by $i\partial/\partial\varphi$ to get

$$H = -E_J \cos \varphi - 4E_C \frac{\partial^2}{\partial\varphi^2}. \quad (13)$$

By analogy with the problem of a particle in a periodic potential the solutions of this Hamiltonian will take the form of Bloch functions.

In the junction there are two energy scales, defined by $E_J = \hbar I_c/2e$ and $E_C = e^2/2C$, which compete. The ratio $E_J/4E_C$ measures the relative importance of the charging energy of the pairs. When E_J is dominant the quantum fluctuations in the phase are small. When $E_J \sim E_C$ the kinetic energy term induces delocalization of the phase. In the other limit, $E_J \ll E_C$ tunneling is weak and large charge transfers are energetically prohibitive (Coulomb blockade).

The classical behavior assumed in Sec. 2.1 corresponds to junctions for which $E_J \gg E_C$. Since E_J increases with the junction area and E_C decreases with the junction area, the classical description fails for small enough junctions, which have small critical currents and large capacitances.

In addition to an appropriate E_J/E_C ratio, in order to observe quantum behavior we need to have the thermal energy $k_B T \ll E_J, E_C$ and large tunneling resistances $R > h/4e^2 = 6.45\text{k}\Omega$ (to avoid quantum fluctuations).⁷

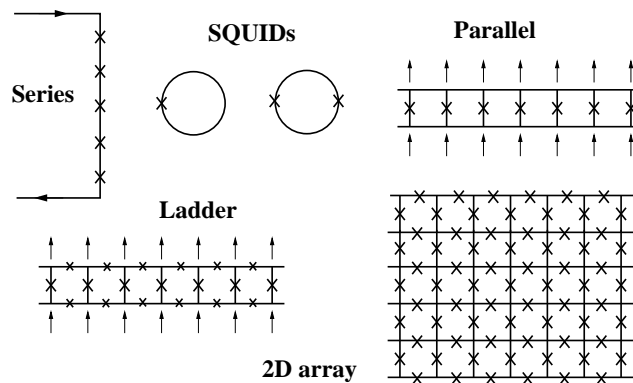


Fig. 8. Sketches of different types of Josephson arrays. Each cross represents a JJ.

Many experimental evidences of quantum mechanical behavior of small JJs were found in the late 80's and 90's. Some of the highlights were: the observation of macroscopic quantum tunneling of the phase and energy level quantization in a single JJ junction.¹⁸ The evidence of single Cooper-pair tunneling.¹⁹ The demonstration of the Heisenberg's uncertainty principle in a superconductor.²⁰ More recently, it has been studied a dissipative quantum phase transition in a single junction,²¹ and the quantum mechanical behavior of a single vortex in a long JJ.²²

We want also to mention the recent works directed to operate with quantum states of single JJs and simple JJ circuits. For instance the achievement of coherent control of macroscopic quantum states in a single-Cooper-pair box.²³ The observation of the quantum superposition of distinct macroscopic states in a rf SQUID²⁴ and a superconducting loop with 3 junctions.²⁵ The manipulation of the quantum state of a superconducting tunnel junction circuit.²⁶ The generation and observation of coherent temporal oscillations between the macroscopic quantum states of a Josephson tunnel junction.²⁷ The report of quantum coherent dynamics of a superconducting flux qubit.²⁸ And the recent observation of quantum oscillations in two coupled charge qubits.²⁹

3. Modeling Josephson arrays

Systems with superconducting wires interrupted by JJs are usually known with the name of JJ arrays. Figure 8 shows examples of such arrays. All of them are easy to fabricate and have been widely studied. The first device consist of a series array of JJs. This type of arrays have been employed for

studying phase locking phenomena and build the voltage standard.³⁰ Superconducting loops interrupted by one or two junctions are known as SQUIDS (for superconducting quantum interference device).^{4,5,31–33} SQUIDS provide a sensitive measure of magnetic flux and today are used as standard magnetic field detector in many laboratories. Parallel arrays have been designed for studying fluxon transport devices but from a fundamental point of view they are interesting because constitute an experimental realization of the Frenkel Kontorova model or the discrete sine-Gordon equation.^{34–38} Ladder arrays were designed for studying the transition from one-dimensional to two-dimensional physics and allowed an experimental observation of discrete breathers,^{39,40} the main topic of this lecture. Two dimensional arrays are an ideal model system to study 2D phase transitions, frustration and disorder effects, vortex dynamics, phase synchronization and other non-linear dynamics results.⁴¹

To derive the equations of the dynamics of the array we have to apply Kirchoff's conservation law (for the current and for the voltage) and fluxoid quantization. Fluxoid quantization condition establishes that for any loop l in the array (with at least one junction) the sum of all the phase differences around the loop is given by

$$\sum_{j \in l} \varphi_j = 2\pi(n_l - f_l). \quad (14)$$

The integer n_l is the vorticity of the loop and results from the multivaluedness of the phase θ of the superconducting wave function in each superconducting island. f_l accounts for the total (external plus induced) flux of the magnetic field through the loop measured in terms of Φ_0 ($f_l = \Phi_l/\Phi_0$). In general, to compute the total induced flux in a cell one must take into account the full inductance matrix of the circuit. However, in many cases we can work with a simpler approximation and consider only the self-inductance L of each cell. The parameter $\lambda = \Phi_0/2\pi I_c L$ measures the importance of the induced fields.

We can leave out the n_l terms^b and write

$$\sum_{j \in l} \varphi_j = -2\pi(f_l^{\text{ext}} + f_l^{\text{ind}}) = -2\pi f_l^{\text{ext}} - \frac{1}{\lambda} \frac{I^{\text{loop}}}{I_c}. \quad (15)$$

^bIn the RCSJ model the dynamical equations depend only on $\ddot{\varphi}$, $\dot{\varphi}$ and $\sin \varphi$. Then the equations of motion are independent of the n_l and we can eliminate them from our equations

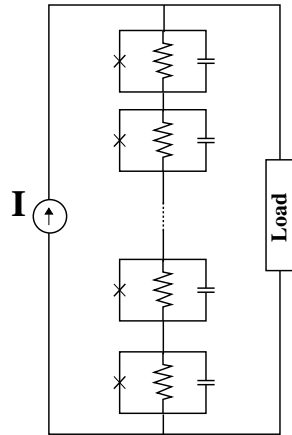


Fig. 9. Biased JJ series array shunted by an external load

Depending on the importance of the induced fields, Josephson circuits can be divided in two general types. Circuits of the first type have $\lambda \gg 1$ so the induced flux in the loop is not important (these circuits are typically made of aluminum). Otherwise the circuits belong to the second type and the flux caused by the circulating currents is important (these circuits are typically made of niobium).

If inductive effects can be neglected, fluxoid quantization (Eq. 14) imposes a constraint to the equations and then reduces the number of independent variables of the system.

3.1. Series arrays

Figure 9 shows a series array of JJs biased by an external current and a load circuit. The equations of the array can be written as⁴²

$$\ddot{\varphi}_k + \Gamma \dot{\varphi}_k + \sin \varphi_k + I_L(t) = I \quad (16)$$

$$V(t) = \sum_{k=1}^N \dot{\varphi}_k = F(I_L(t)). \quad (17)$$

Thus, the junctions behave as independent elements biased by the same current and coupled through the load circuit.

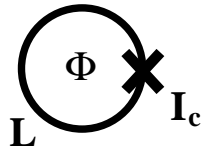


Fig. 10. rf-squid device

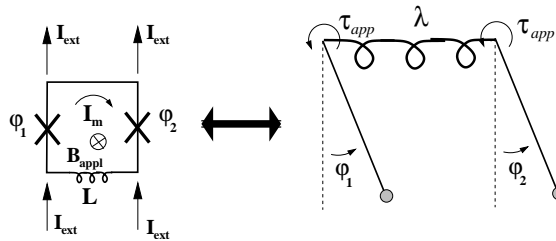


Fig. 11. dc-squid device and equivalence with the two coupled pendula system.

3.2. rf-SQUID

This device consists of a superconducting loop with a single JJ in it (Fig. 10). The behavior is governed by the value of total flux through the SQUID, Φ . From the fluxoid quantization condition $\varphi = -2\pi \frac{\Phi}{\Phi_0}$. Then,

$$\Phi = \Phi_{\text{ext}} - LI_c \sin 2\pi \frac{\Phi}{\Phi_0} \quad (18)$$

and the potential energy of the system is given by

$$U(\Phi) = -E_J \cos 2\pi \frac{\Phi}{\Phi_0} + \frac{(\Phi - \Phi_{\text{ext}})^2}{2L}. \quad (19)$$

Since in this circuit there is no bias current, the rf-SQUID is operated coupled to a radio-frequency circuit (resonator).

In addition to magnetic flux measurements rf-SQUIDS are important for the study of fundamental problems on quantum mechanics (see Ref. 24 and references within).

3.3. dc-SQUID

This device consists of a superconducting loop with two JJs (Fig. 11). Now current conservation reads:

$$\begin{aligned} i_1 &= \ddot{\varphi}_1 + \Gamma \dot{\varphi}_1 + \sin \varphi_1 = i^{\text{mesh}} + i_{\text{ext}}, \\ i_2 &= \ddot{\varphi}_2 + \Gamma \dot{\varphi}_2 + \sin \varphi_2 = -i^{\text{mesh}} + i_{\text{ext}}; \end{aligned} \quad (20)$$

and fluxoid quantization:

$$(\varphi_1 - \varphi_2) = -\frac{2\pi}{\Phi_0} (B_{\text{appl}}S + LI^{\text{mesh}}). \quad (21)$$

Normalizing, we get

$$i^{\text{mesh}} = -\lambda(\varphi_1 - \varphi_2 + 2\pi f_0) \quad (22)$$

($f_0 = B_{\text{appl}}S/\Phi_0$).

Then the equations for the dynamics of the array are

$$\begin{aligned} \ddot{\varphi}_1 + \Gamma\dot{\varphi}_1 + \sin \varphi_1 &= -\lambda(\varphi_1 - \varphi_2 + 2\pi f_0) + i_{\text{ext}} \\ \ddot{\varphi}_2 + \Gamma\dot{\varphi}_2 + \sin \varphi_2 &= \lambda(\varphi_1 - \varphi_2 + 2\pi f_0) + i_{\text{ext}}. \end{aligned} \quad (23)$$

Where $I_{\text{ext}}=I_{\text{total}}/2$. These equations show that the problem of two junctions connected in parallel by an inductive element is equivalent to the problem of two pendula coupled by a torsion spring (see Fig. 11).

If inductive effects can be neglected, fluxoid quantization imposes a constraint on the variables and we have that

$$\varphi_1 - \varphi_2 = -2\pi f_0. \quad (24)$$

Then, current conservation reads

$$i_{\text{ext}} = \frac{i_1 + i_2}{2} = \ddot{\varphi}_1 + \Gamma\dot{\varphi}_1 + \cos(\pi f_0) \sin(\varphi_1 + \pi f_0). \quad (25)$$

The system behaves like a single junction with the critical current modulated by the external field.

3.4. JJ parallel array

A JJ parallel array is formed by a set of junctions connected in parallel by superconducting wires. The mechanical analog for this system is a set of pendula connected by torsion springs (see Fig 12). An important consequence of this harmonic interaction is that all the junction must have the same dc voltage.

The equations for the array can be easily generalized from the dc SQUID. For the parallel array we get,

$$\ddot{\varphi}_j + \Gamma\dot{\varphi}_j + \sin \varphi_j = \lambda(\varphi_{j+1} - 2\varphi_j + \varphi_{j-1}) + i_{\text{ext}} \quad (26)$$

with $j = 1, \dots, N$. The boundary conditions are given by $\varphi_0 = \varphi_1 - 2\pi f_0$ and $\varphi_{N+1} = \varphi_N + 2\pi f_0$ for the case of open-ended arrays and $\varphi_{N+1} = \varphi_1 + 2\pi n_k$ and $\varphi_0 = \varphi_N - 2\pi n_k$ for ring arrays. In this last case the integer n_k computes the number of kinks or fluxons trapped in the array.

Equations (26) are also the equations of the dynamics of the forced and damped Frenkel-Kontorova model or the discrete sine-Gordon equation.

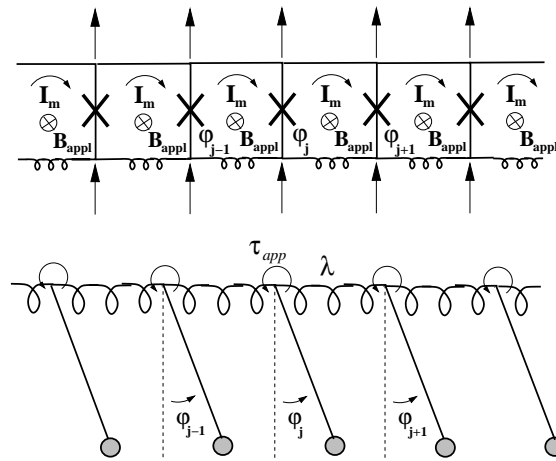


Fig. 12. JJ parallel array

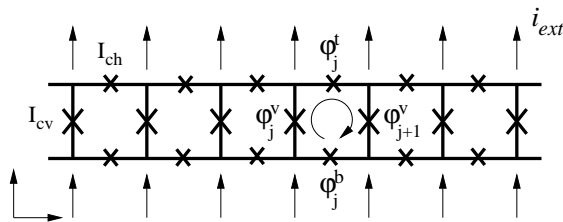


Fig. 13. JJ ladder array

3.5. JJ ladder array

A Josephson ladder array (Fig. 13) is a quasi-one-dimensional array made when the superconducting horizontal wires of the parallel array are interrupted by Josephson junctions. We can think of this system as a set of pendula (the vertical junctions) connected in parallel by nonconvex springs (the horizontal junctions). Consequence of the non-convex interaction, one of the more notable differences with respect to the parallel array is that now the vertical junctions are not constrained to have the same dc voltage. Also, now fluxoid quanta can go into and escape from the array through the horizontal junctions.

Let us consider the case of an anisotropic ladder. Then the critical current of junctions in the vertical direction is different from the critical current of junctions in the horizontal direction. It can be easily made by changing

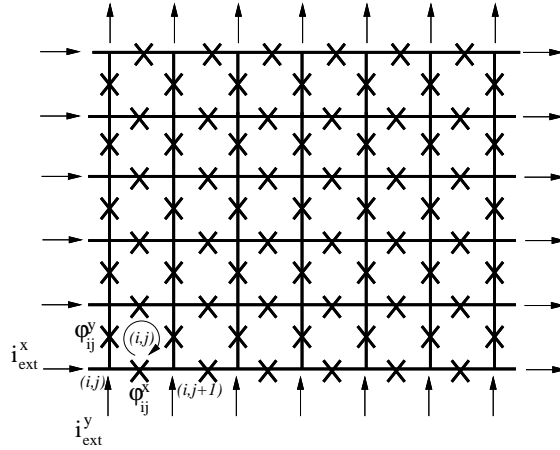


Fig. 14. 2D JJ array

the area of the junctions. Critical current and capacitance are proportional to this area and resistance is inversely proportional to the area.

Applying current conservation and fluxoid quantization, the equations for the ladder read

$$\begin{aligned}\mathcal{N}(\varphi_j^t) &= -\frac{\lambda}{h}\xi_j, \\ \mathcal{N}(\varphi_j^v) &= \lambda(\xi_{j-1} - \xi_j) + i_{\text{ext}}, \\ \mathcal{N}(\varphi_j^b) &= \frac{\lambda}{h}\xi_j.\end{aligned}\quad (27)$$

Here we have defined

$$\xi_j = -2\pi f_j^{\text{ind}} = \varphi_j^v + \varphi_j^t - \varphi_{j+1}^v - \varphi_j^b + 2\pi f_0, \quad (28)$$

where $\xi_0 = \xi_N = 0$. For a ladder with N vertical junctions, j runs from 1 to N for vertical junctions and from 1 to $N - 1$ for horizontal ones. We have normalized with respect to the parameters of the vertical junctions. Thus, $h = I_{ch}/I_{cv} = C_h/C_v = R_v/R_h$ and $\lambda = \lambda_v = \Phi_0/2\pi I_{cv}L$ ($\lambda/h = \lambda_h = \Phi_0/2\pi I_{ch}L$).

3.6. 2D arrays

Figure 14 shows a sketch of a square 2D Josephson array. Following our approach to model Josephson arrays, the junctions are coupled via the flux quantization condition with the inclusion of cell self induced magnetic fields.

In this approach, the equations for the dynamics of the array are:

$$\begin{aligned}\mathcal{N}(\varphi_{ij}^x) &= \frac{\lambda}{h}(\xi_{ij} - \xi_{ij-1}) + \frac{i_x^{\text{ext}}}{h}, \\ \mathcal{N}(\varphi_{ij}^y) &= \lambda(\xi_{i-1j} - \xi_{ij}) + i_y^{\text{ext}}\end{aligned}\quad (29)$$

ξ_{ij} measures the intensity of the induced field

$$\xi_{ij} = -2\pi f_{ij}^{\text{ind}} = \varphi_{ij}^y + \varphi_{ij+1}^x - \varphi_{i+1j}^y - \varphi_{ij}^x + 2\pi f_0 \quad (30)$$

and we have normalized with respect to the parameters of the y junctions. Thus $h = I_{cx}/I_{cy} = C_x/C_y = R_y/R_x$ and $\lambda = \lambda_y = \Phi_0/2\pi I_{cy}L$ ($\lambda/h = \lambda_x = \Phi_0/2\pi I_{cx}L$).

This is a model for a 2D array when only self-inductances are taken into account. Sometimes, depending on the problem to be studied, inductances are not needed at all; in some others a full inductance matrix is necessary.

In general, in a square 2D ($N \times N$) array we have to solve equations for the dynamics of $2N^2 - 2N$ (for free boundary conditions) gauge-invariant phase differences, φ_{ij} . However, when induced fields can be neglected ($\lambda \gg 1$ limit), flux quantization condition imposes $(N-1)^2$ constraints on these variables. Then, it is more convenient to express the system equations in terms of the phase in each island, θ_i , which are $N^2 - 1$ independent variables. This is made by writing $\varphi_{ij} = \theta_i - \theta_j - A_{ij}$ [where (for a given gauge) the $A_{ij} = \frac{2\pi}{\Phi_0} \int_i^j \vec{A}(\vec{r}, t) \cdot d\vec{l}$, depend only on the external magnetic field] and the dynamical equations result after applying current conservation.

In the $E_J \gg E_C$ limit of the system the total Josephson energy is the relevant energy contribution:

$$H_J = - \sum_{\langle ij \rangle} E_J \cos(\theta_i - \theta_j - A_{ij}). \quad (31)$$

In the opposite limit of ultrasmall junctions ($E_C \gg E_J$), the charging energy is the more important contribution:

$$H_Q = \frac{1}{2} \sum_{ij} (Q_i + q_i) C_{ij}^{-1} (Q_j + q_j) \quad (32)$$

where Q_j is the charge in island j , q_j are possible offset charges or charges induced by external sources (charge frustration) and C is the capacitance matrix of the circuit.

The more complex case is that of intermediate values where both terms

should be considered ^c and

$$H = \frac{1}{2} \sum_{ij} (Q_i + q_i) C_{ij}^{-1} (Q_j + q_j) - \sum_{\langle ij \rangle} E_J \cos(\theta_i - \theta_j - A_{ij}). \quad (33)$$

4. Localized excitations in Josephson arrays: vortices and kinks

In this section we are going to summarize some aspects of the physics of vortices in 2D Josephson arrays and kinks in Josephson parallel arrays. Both are broad topics and we do not intend to review them here. A nice review with many references on the physics of 2D Josephson-junction arrays which extensively covers the role of vortices can be found in Ref. 41 For an introduction to the study of kinks in parallel arrays and similar systems see Refs. 34-38

4.1. Vortices in 2D arrays

Consider a two-dimensional array of $N \times N$ superconducting islands coupled by Josephson junctions. The relevant energy of the array is the sum of the Josephson energies of the junctions, which (in the absence of magnetic fields) is given by:

$$H_J = - \sum_{\langle ij \rangle} E_J \cos(\theta_i - \theta_j). \quad (34)$$

This is the Hamiltonian of the two-dimensional XY model and thus 2D JJ arrays are a physical realization of this model. The XY model describes many systems but is particularly interesting because it shows the Kosterlitz-Thoules-Berezinski (KTB) phase transition. Thus, many of the theoretical and experimental works with 2D arrays are focused in the observation and study of this type of phase transition.⁴¹

The linear excitations of Hamiltonian (34) are known as spin waves. They correspond to small amplitude and energy wave-like variations of the phase over the array. In addition to them, the system supports large energy nonlinear excitations that are called vortices (and antivortices). A vortex (see Fig. 15) is an energy localized solution defined by the value of the total phase differences along a path containing the vortex, which is equal to 2π (-2π for antivortices) [For a vortex (antivortex), $\sum(\theta_i - \theta_j) = \pm 2\pi$].

^cThe inclusion of self-induced magnetic fields would give an additional contribution to the hamiltonian of the array

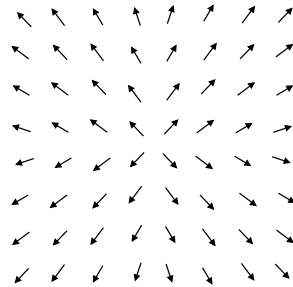


Fig. 15. Sketch of a vortex configuration in a Josephson array. Arrows represent phase of superconducting islands.

4.1.1. *Single vortex properties at zero temperature*

Vortices and antivortices are topological excitations and behave like opposite charges in a two-dimensional system. The ground state configuration for Hamiltonian (34) correspond to the configuration $\{\theta_i\} = \text{const}$. For a large array this configuration has an energy $E = -2N^2E_J$. We can calculate also the energy of an isolated vortex in a large square array of size $L=Na \rightarrow \infty$, which is $E = \pi E_J \ln L/a - 2N^2E_J$.

In the presence of external fields the vortex has a marked single-particle behavior. When an external current is uniformly applied to the array the vortex sees an effective Lorenz-type force perpendicular to the applied current, of magnitude $F_V = (\Phi/2\pi)(I_{\text{tot}}/Na)$. Due to the discreteness of the array, there exist an energy barrier that the vortex has to overcome before moving trough the array. This barrier is the Peierls-Nabarro barrier for the vortex and has a value of $E_{PN} = 0.2E_J$ for square cells and $E_J = 0.043E_J$ for triangular ones. When the vortex moves along the lattice it experiences a two-dimensional Peierls-Nabarro potential. The potential along the x direction $U_{PN} \simeq -(E_{PN}/2) \cos 2\pi x/a$. Following this picture we can compute the vortex depinning current $I_{cV} = (\pi/\Phi_0)E_{PN} = 0.1I_c$, for the square array.

In many cases we can describe the motion of a vortex in the array with an effective equation for the center of the vortex which includes an external force (caused by the external current), a viscous force (power dissipated in the resistive channels), kinetic energy (stored in the capacitors) and potential energy (Josephson energy):

$$I = I_{cV} \sin\left(\frac{2\pi x}{a}\right) + \frac{\Phi_0}{4\pi R} \frac{d(2\pi x/a)}{dt} + \frac{\Phi_0 C}{4\pi} \frac{d^2(2\pi x/a)}{dt^2}. \quad (35)$$

4.1.2. Array properties at non-zero temperatures

The energy that we need to put a vortex into a large array in its ground state is $E_V = \pi E_J \ln L/a$. This energy diverges with the size of the array and thus there are not free vortices in the system at low enough temperatures. However, as soon as $T \neq 0$, the thermal generation of bound vortex-antivortex pairs is energetically favored since the energy to create one of these pairs behave as $E_p = 2\pi E_J \ln r/a$, with r the distance between the vortex and anti-vortex cores. Increasing the temperature we reach the KTB phase transition, $T_{KT} \sim \pi E_J / 2k_B$ where vortex-antivortex pairs unbind and free vortices are present in the array.

Such temperature can be estimated with a simple argument. If we add a single vortex to the array the free energy changes in

$$\Delta F_V = E_V - T\Delta S_V = \pi E_J \ln L/a - k_B T \ln (L/a)^2, \quad (36)$$

here $(L/a)^2$ is the number of places where we can put the vortex in the array. ΔF_V becomes zero at $T = \pi E_J / 2k_B$.

This is the simplest description of the physics of the system. In general the results are affected by the inclusion of external magnetic fields, finite size-effects, self-induced fields, disorder,... In any of the cases the concept of vortex is essential to understand the physics of the array.

4.2. 2D arrays with small junctions

In arrays of ultrasmall tunnel junctions the relevant energy is the charging energy,⁴³

$$H_Q = \frac{1}{2} \sum_{ij} Q_i C_{ij}^{-1} Q_j \quad (37)$$

where Q_i is the charge in the island. For metallic “normal state” islands this charge is an integer multiple of the electronic charge e . In the superconducting state, at low temperatures and voltages below the gap voltages, Cooper pairs are dominant and the charge appears in multiples of $2e$.

In any of the cases (normal or superconducting arrays) at zero temperature no free charges are present in the array. The system is insulating. In arrays where mutual capacitances are dominant the charges interact logarithmically over long enough distances. Then, free charges are expected to be created by thermal activation through a KTB phase transition where pairs of opposite charges unbind, and the array becomes resistive. The estimated temperature for the transition is $T_{cn} = E_C / 4\pi k_B$ for normal islands

and $T_{cs} = E_C/\pi k_B$ for superconducting ones ($E_C = e^2/2C$). In real circuits this transition is strongly affected by dissipation [measured by the coefficient $\alpha_T = h/(4e^2 R_T)$], presence of offset charges, disorder,...

In small capacitance superconducting junctions we have to include both the charging and the Josephson coupling. If we ignore quasiparticles, the Hamiltonian of the system is

$$H = \frac{1}{2} \sum_{ij} Q_i C_{ij}^{-1} Q_j - \sum_{\langle ij \rangle} E_J \cos(\theta_i - \theta_j), \quad (38)$$

where we have ignored also charge or phase frustration (offset or induced charges and magnetic fields).

If charging energy can be neglected ($E_C=0$ limit) the vortices undergo a KTB transition where vortex dipoles unbind. This transition separates a superconducting low temperature phase from a resistive high temperature one. If the Josephson coupling is weak ($E_J=0$ limit), the charges show a KTB transition where the dipoles, formed by a Cooper pair and a missing pair, unbind. The transition separates an insulating from a conducting phase.

At finite E_J and E_C , both charge and vortex excitations have to be considered simultaneously. The charging energy provides a kinetic energy for the vortices, and the Josephson coupling allows the tunneling of Cooper pairs and provides dynamics for the charges. If $E_C \ll E_J$ or $E_J \ll E_C$ perturbative approaches can be used.

However, to fully understand the physics of the system we have to consider also the influence of the quasiparticle tunneling. We have a quantum dissipative system.

We have also seen that vortices can be described as particles moving in a substrate potential with a mass given by the charging energy. For small junctions we can expect strong quantum mechanical effects. At finite temperatures vortex motion can be thermally excited. At low temperatures it is possible to observe quantum mechanical tunneling of vortices.

A review on quantum phase transitions and vortex dynamics in superconducting networks can be found in Ref. 44

4.3. *Kinks in parallel arrays*

We have seen in Sec. 3.4 that the equations for the dynamics of a parallel array of JJs correspond to the equations of the dynamics of the Frenkel-Kontorova model or the discrete sine-Gordon equation. Reviews of the physics of these systems are Refs. 34-36

The equations for the dynamics of the junctions in the parallel array are given by

$$\ddot{\varphi}_j + \Gamma \dot{\varphi}_j + \sin \varphi_j = \lambda (\varphi_{j+1} - 2\varphi_j + \varphi_{j-1}) + i_{\text{ext}} \quad (39)$$

(with $j = 1, \dots, N$ and boundary conditions are $\varphi_0 = \varphi_1 - 2\pi f_0$ and $\varphi_{N+1} = \varphi_N + 2\pi f_0$ for an open array and $\varphi_{N+1} = \varphi_1 + 2\pi n_k$ and $\varphi_0 = \varphi_N - 2\pi n_k$ for a ring. n_k is the number of kinks or fluxons trapped in the ring).

The system supports different types of excitations. Linear waves are small amplitude and energy wave-like variations of the phase over the array. When the phases are small, the solution of the linearized equations (for zero damping and current) is: $\varphi_j(t) \sim \exp(i(\omega_k t - k j))$ with

$$\omega_k^2 = 1 + 4\lambda \sin^2(k/2) \quad (-\pi < k \leq \pi). \quad (40)$$

This dispersion relation is characterized by a finite band with gap $\omega_{\min} = \omega_0 = 1$ and maximum frequency $\omega_{\max} = \omega_\pi = (1 + 4\lambda)^{1/2}$.

When the phases are not small the linear approximation is not valid and the dynamics is pretty rich supporting new type of localized excitations: kinks and breathers

Kinks and anti-kinks are the only excitations which can exist in the array in the static case. Depending on the context, they are also called discrete solitons or elementary discommensurations. They correspond to solutions where the phases go from 0 to $2\pi(-2\pi)$ along the array. Since $(\varphi_{j+1} - \varphi_j) = -2\pi\Phi_j/\Phi_0$; then $(\varphi_N - \varphi_1) = 2\pi = -2\pi\Phi_{\text{tot}}/\Phi_0$ and one kink corresponds to one fluxon of magnetic field.

The existence of kinks does not depend crucially on the discreteness of the system. Moreover, in many aspects the kinks are similar to the solitons found in the continuous version of the equation (the sine-Gordon equation). However, many other properties of the kinks do depend crucially on the discreteness of the array. The existence of a discrete lattice breaks the invariance under continuous translations of the solitons of the continuous model. In the lattice, the kink is invariant only under discrete translations along the array and, due to discreteness, the kink is pinned to the lattice: there exists a minimum energy barrier the kink needs to overcome in order to move through the lattice. This energy is the so-called Peierls-Nabarro (PN) barrier (Fig. 16) and decreases rapidly with λ (Fig. 17).

We can go further and define not only a PN barrier but also a PN potential for the kink. To compute the kink potential profile we let the kink configuration to relax following the overdamped dynamics,

$$\dot{\varphi}_j = -\sin \varphi_j + \lambda (\varphi_{j+1} - 2\varphi_j + \varphi_{j-1}), \quad (41)$$

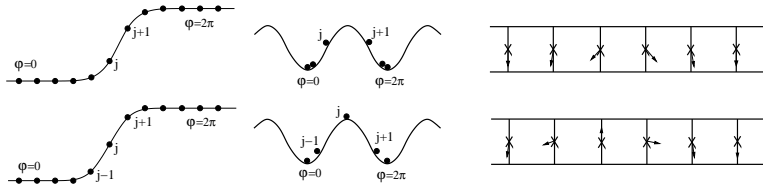


Fig. 16. Three different representations of the minimum energy configuration (top figures) and the saddle configuration, maximum of the PN potential, of a kink in the parallel array (bottom figures): phase representation (left), potential energy representation (center) and angular representation (right).

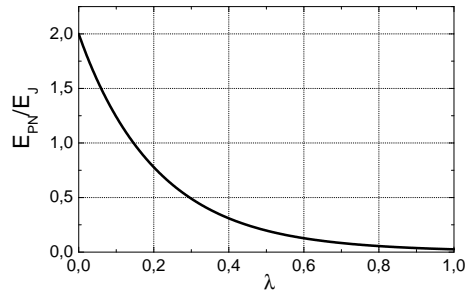


Fig. 17. E_{PN} vs the coupling parameter λ for a kink in the parallel array.

from the saddle-point configuration to the minimum energy configuration. During the relaxation we work out the energy,

$$E/E_J = \sum_j \left[(1 - \cos \varphi_j) + \frac{\lambda}{2} (\varphi_{j+1} - \varphi_j)^2 \right], \quad (42)$$

and center of mass,

$$X_{CM} = C \pm \sum_j \varphi_j, \quad (43)$$

of the configuration obtaining the potential profile $E(X_{CM})$.

In some cases is possible to identify the kink motion with the motion of a single particle over a sinusoidal periodic potential defined by:

$$V_{PN}(X) = \frac{E_{PN}}{2} (1 - \cos X). \quad (44)$$

In the presence of external bias, an effective equation of motion for the kink is given by

$$m\ddot{X} + m\Gamma\dot{X} + \frac{E_{PN}}{2} \sin X = i. \quad (45)$$

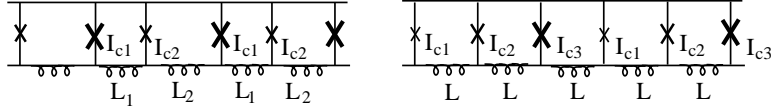


Fig. 18. Two different designs of parallel arrays where fluxons experience a ratchet periodic potential.

The picture of the kink or fluxon as a single particle is particularly useful in arrays which are larger than the fluxon width and are driven by small currents (far from the whirling mode).

When the kink moves it radiates energy in form of small amplitude waves. This radiation is very strong for the case of underdamped arrays. There, phonons are easily excited by the kink in its wake and resonances between the kink velocity and these waves appear.^{37,38}

A particularly interesting configuration is a ring of JJ connected in parallel. There, once the array is superconducting magnetic field gets trapped as an integer number of fluxons.

4.3.1. Fluxon ratchet potentials

We have considered arrays where all the junctions are identical and all the cells have the same size. However, it is possible to design different arrays which are adequate for studying new physical problems.

One example is the use of Josephson parallel arrays to study the dynamics of kinks subjected to substrate ratchet potentials.⁴⁷⁻⁴⁹

A ratchet potential is a periodic potential without inversion symmetry: $V(x) \neq V(-x)$, then it is easier to move a particle in one direction than in the other.

The equations for a non-uniform array (made of junctions with different areas and cells of different sizes) are

$$h_j (\ddot{\varphi}_j + \Gamma \dot{\varphi}_j + \sin \varphi_j) = \lambda_j (\varphi_{j+1} - \varphi_j) - \lambda_{j-1} (\varphi_j - \varphi_{j-1}) + i_{\text{ext}} \quad (46)$$

with $h_j = I_{c_j}/I_c^* = C_j/C^* = R^*/R_j$, where the * superscript stands for the parameters of the junction with respect to which we normalize, and $\lambda_j = \Phi_0/2\pi I_c^* L_j$.

A kink ratchet potential can be obtained with different suitable combinations of junctions and inductance. The simplest ones (see Fig. 18) are made alternating junctions of two critical currents and cells of two areas, and alternating junctions of three critical currents.

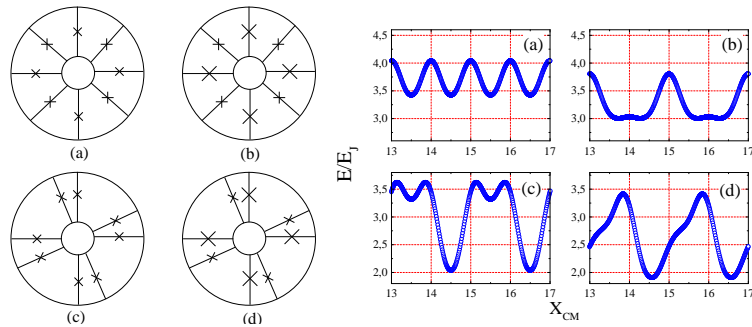


Fig. 19. Four studied arrays: (a) regular ring, (b) ring with alternating critical currents, (c) ring with with alternating cell areas, (d) ratchet ring with alternating critical currents and cell areas; and the corresponding energy profiles $E(X_{CM})$. Only configuration (d) gives a ratchet profile.

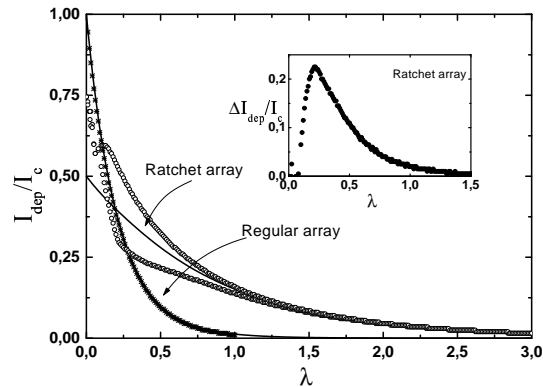


Fig. 20. Fluxon depinning currents I_{dep} as a function of λ for the regular and ratchet arrays. Solid lines stand for predictions from E_{PN} values and symbols stand for numerical computation of the depinning currents.⁴⁹ The inset show the difference (ΔI_{dep}) between the absolute values of the two depinning currents for the ratchet array.

Figure 19 shows four different arrays and the computed PN potentials. As we should expect only array (d) shows a ratchet fluxon potential. Such arrays were built and experimentally studied.⁴⁸

Figure 20 shows the dependence as a function of λ of the positive and negative values of the fluxon depinning current (the minimum current to move the fluxon) for the cases of the regular and ratchet arrays.⁴⁹ We see that for the ratchet array I_{dep}^+ and I_{dep}^- are significantly different for values of λ between 0.1 and 0.9. The inset shows the difference ($\Delta I_{dep} = I_{dep}^- - I_{dep}^+$)

between the values of the two depinning currents for the ratchet array. As we can see there exist a moderate range of values of λ for which an important ratchet behavior is expected. The maximum of this curve is obtained for $\lambda \sim 0.2$.

4.4. Charge solitons in 1D arrays

We want to mention also the case of a one-dimensional array of ultra-small junctions. There the Josephson coupling is weak, $E_J \ll E_C$ and the normal resistance large $R > h/4e^2$.

Then, if a single electron (or a single pair) is added to or subtracted from an intermediate island the resulting localized state, the single charge plus the polarization cloud, is called charge soliton (or anti-soliton). It corresponds to a localized voltage profile and some of their properties have been studied by means of the sine-Gordon equation.^{45,46}

5. Discrete breathers in Josephson arrays

Discrete breathers^{50–54} excitations (also called intrinsic localized modes) are solutions of the dynamics of nonlinear lattices for which the energy remains exponentially localized in a few sites of the array. As we have seen, Josephson arrays are ideal experimental discrete system to study nonlinear dynamics, thus much effort in the last years has been devoted to the prediction and experimental observation^{55,56} of discrete breathers in Josephson arrays. E. Trías and P. Binder wrote their thesis on this subject^{57,58} and some recent review articles are Refs.^{39,40,59}

Josephson circuits are externally biased dissipative systems. Thus, the breather solutions that we are going to present are attractors of the dynamics of the array. We will distinguish between two types of localized modes: oscillobreathers, where all the phases oscillate (a few of them with large amplitude and the rest with small amplitude); and rotobreathers where most phases oscillate but some other rotate. Since the main object is to experimentally study the modes, much effort has been put in the study of rotobreathers because they show a dc signal. The plasma frequency for a Josephson junction is close to 100GHz. Thus it is not possible to follow the instantaneous dynamics of the phases. A quantity easy to measure however is the dc voltage of the junction (only rotating junctions have nonzero dc voltage).

An approach to the study of DB solutions is to build the breather from some appropriate uncoupled limit (which is not going to be experimentally

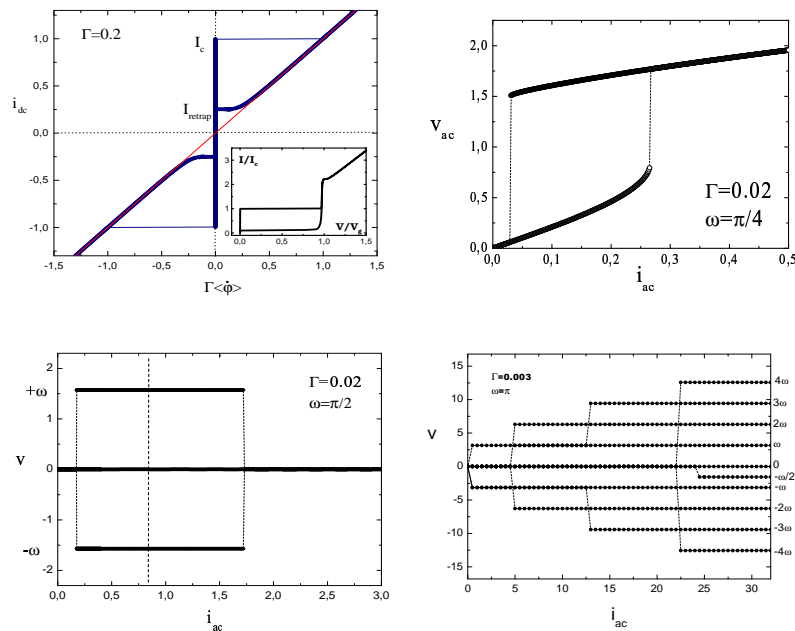


Fig. 21. Simulation of IV curves for a single junction with a linear resistor: (a) DC bias, $\Gamma = 0.2$ (inset: experimental curve showing the gap voltage branch). (b-d) Underdamped junction biased by an rf field. (b) $\Gamma = 0.02$ and $\omega = 2\pi \times 0.125$, at a certain value of the amplitude of the field, an “small” amplitude oscillating state destabilizes to a “large” amplitude one. Both states coexist for certain range of values of i_{ac} . (c) $\Gamma = 0.02$ and $\omega = 2\pi \times 0.25$, for a certain range of values of i_{ac} an oscillating state coexist with two rotating states with $\langle\dot{\phi}\rangle = \pm\omega$. (d) $\Gamma = 0.003$ and $\omega = 2\pi \times 0.5$, depending on the value of i_{ac} different attractors coexist with rotation velocities in general given by $\langle\dot{\phi}\rangle = \frac{n}{m}\omega$. (The figure shows only one of the possible subharmonic ($m > 1$) states).

accessible) of the model. The idea is to set one of the junctions in a dynamical state, the other in a different one and then switch on the coupling. All junctions are identical and see the same external force. Thus we are going to start by exploring the dynamics of a single junction looking for regions where two or more states can coexist.

Figure 21(a) shows an IV curve for an underdamped junction (RCSJ model) in the presence of dc bias. We see that for currents between I_c and I_{ret} two different solutions are possible. One of them is a superconducting (zero voltage) state, the other a resistive one. The inset shows a measured IV curve (see also Fig. 5). In a range of external currents two states, with $V=0$ and $V=V_g$, coexist.

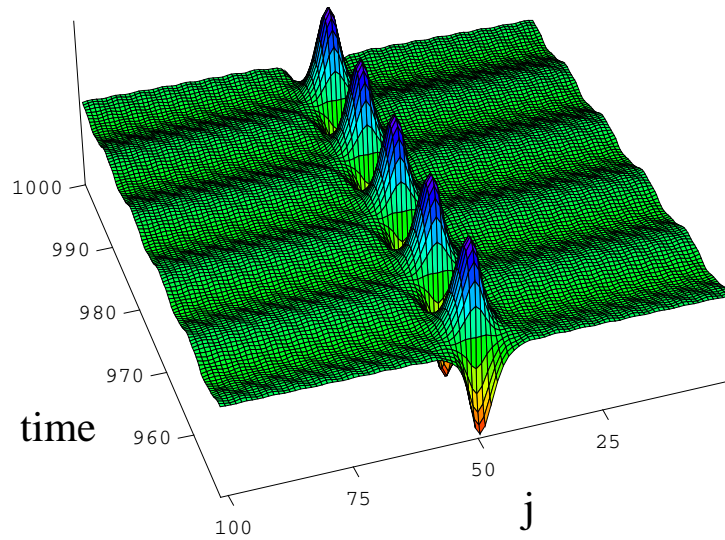


Fig. 22. Numerical simulation of an oscillobreather solution in an ac biased Josephson parallel array

Figures 21(b-d) show IV curves for an underdamped junction (RCSJ model) in the presence of ac bias, $i(t) = i_{ac} \sin(\omega t)$. (b) shows a situation where two solutions with zero dc voltage but different amplitude coexist. The dc voltage is zero so we plot $v_{ac} = \sqrt{\langle \dot{\varphi}^2 \rangle - \langle \dot{\varphi} \rangle^2}$, which measures the oscillation amplitude. (c) and (d) show situations where non-zero dc voltage solutions coexist with a zero voltage one. The junction voltage is synchronized to the frequency of the external field and, in the general case, $\langle \dot{\varphi} \rangle = \frac{n}{m} \omega$.

5.1. Oscillobreather in an ac biased parallel array

The simplest Josephson array with breathers is the parallel array, which is described by a discrete sine-Gordon equation. This system supports only oscillobreather solutions. They are attractors of the dynamics of the array biased by ac external currents. In the breather one junction describes a large amplitude oscillation meanwhile the other follow the external force and oscillates with a small amplitude. Figure 22 shows a picture of an oscillating discrete breather solution in a Josephson parallel array. In the parallel array all the junctions have the same dc voltage ($V=0$ in the oscillobreather solution) since they are connected by superconducting wires.

Oscillobreather solutions can be excited in other Josephson arrays. However, due to the high frequencies involved in the Josephson effect, the oscillobreathers are very hard to experimentally detect. Thus, the experimental effort and much of the theoretical one have been focused to study rotobreathers.

5.2. *Rotobreathers in Josephson arrays*

A rotobreather corresponds to a solution where one junction rotates ($V \neq 0$) meanwhile the others oscillate ($V=0$). This is a voltage localized solution in the array. Such state is easy to detect by measuring the local dc voltages throughout the array. Another important advantage of the rotobreather states is that in principle they can be obtained by either biasing the array with ac currents or with a dc current. This last possibility requires a simpler experimental approach.

One may wonder if these rotating localized modes exist in JJ parallel arrays. In principle, they exist in the uncoupled limit of the model. However, the convex character of the coupling between junctions in the array shows that any localized mode will not be stable since the difference between neighboring phases can not grow without limits. Physically, in a parallel array the dc voltage is the same for all the junctions since they are connected by superconducting leads, thus preventing dc voltage localized solutions. To have rotobreathers in Josephson arrays we will need non-convex interaction terms between neighbors.

The simplest manner to overcome this difficulty is to substitute the horizontal wires connecting neighboring junctions by new Josephson elements. Such a new configuration is known as Josephson ladder.

5.3. *The ladder array*

From our perspective a Josephson ladder can be thought of as a set of parallel pendula, the vertical junctions, coupled by sinusoidal terms (the non-convex terms) provided by the horizontal junctions. The intensity of the coupling is governed by the ratio of the critical current for the horizontal junctions I_{ch} to the critical current for the vertical junctions I_{cv} . Thus, it is natural to study anisotropic ladders where the anisotropy is controlled by the parameter $h = I_{ch}/I_{cv}$. A large value of h means that coupling between vertical junctions will be strong meanwhile a small value of h means weakly coupled vertical junctions. Anisotropic arrays are fabricated by varying the area of the junctions. Critical current and capacitance are proportional

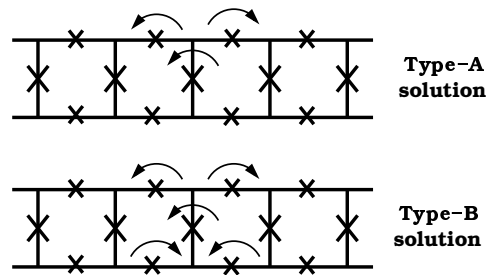


Fig. 23. Two different voltage patterns for a one-site rotobreather in a Josephson ladder. Arrows represent rotating junctions, junctions with dc voltage different from zero.

to this area and the resistance is inversely proportional to it. Thus, also $h = C_h/C_v = R_v/R_h$ and the damping Γ and the plasma frequency ω_p are the same for all the junctions.

We want to recall the equations for the system, introduced in Sec. 3.5:

$$\begin{aligned}
 \mathcal{N}(\varphi_j^t) &= -\frac{\lambda}{h}\xi_j \\
 \mathcal{N}(\varphi_j^v) &= \lambda(\xi_{j-1} - \xi_j) + i_{\text{ext}} \\
 \mathcal{N}(\varphi_j^b) &= \frac{\lambda}{h}\xi_j.
 \end{aligned} \tag{47}$$

Where we have defined

$$\xi_j = -2\pi f_j^{\text{ind}} = \varphi_j^v + \varphi_j^t - \varphi_{j+1}^v - \varphi_j^b + 2\pi f_0, \tag{48}$$

and normalized with respect to the parameters of the vertical junctions, thus $h = I_{ch}/I_{cv} = C_h/C_v = R_h/R_v$ and $\lambda = \lambda_v = \Phi_0/2\pi I_{cv}L$ and $\lambda/h = \lambda_h = \Phi_0/2\pi I_{ch}L$.

5.4. Rotobreathers in a dc biased ladder

The simplest rotobreather solutions in a dc biased ladder array are shown in Fig. 23. One vertical junction and some of its neighbors are excited at the gap voltage meanwhile the other oscillate around the superconducting state. Such solutions can be continued from the uncoupled limit or excited by adding local dc currents to the central junction.⁶⁰

The rotobreathers in the ladder can be unambiguously detected by measuring local dc voltages and have been found in numerical simulations of the model and experimentally observed. Other more complex patterns and multi-site DB solutions have been also excited and detected.^{61–63} Multi-site

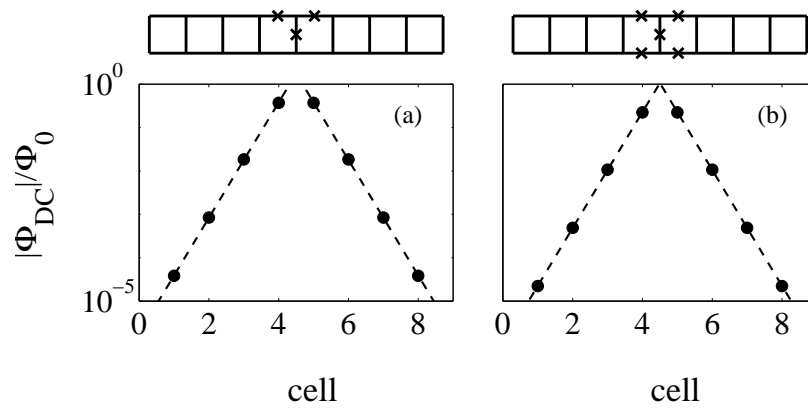


Fig. 24. Simulation of 9×1 array with $\lambda = 0.05$, $\Gamma = 0.1$ and $h = 0.25$. We have plotted the absolute value of the DC flux per unit cell at $I = 0.7$. The flux decays exponentially with a decay length of 0.32 for both solutions.

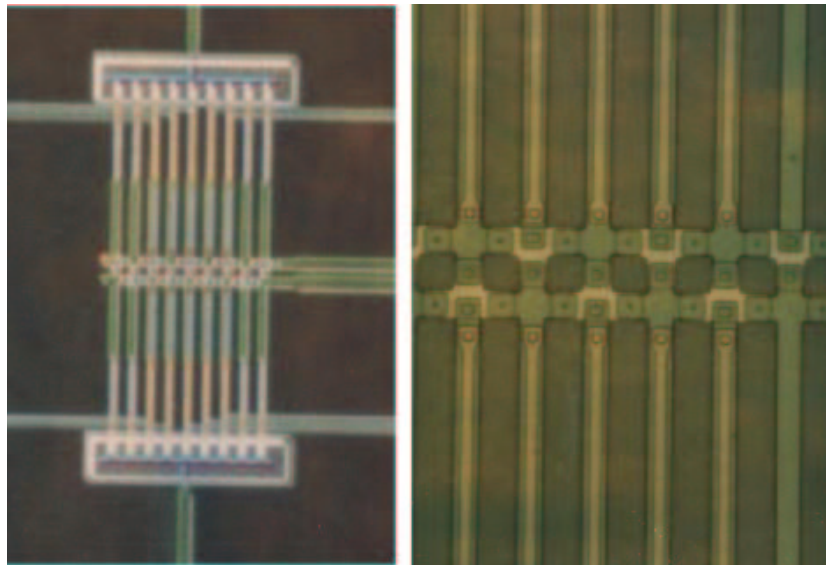


Fig. 25. Picture of the ladder

solutions are characterized by a breather core with more than one rotating vertical junction.

Figure 24 shows the absolute value of the dc flux per unit cell for a type-

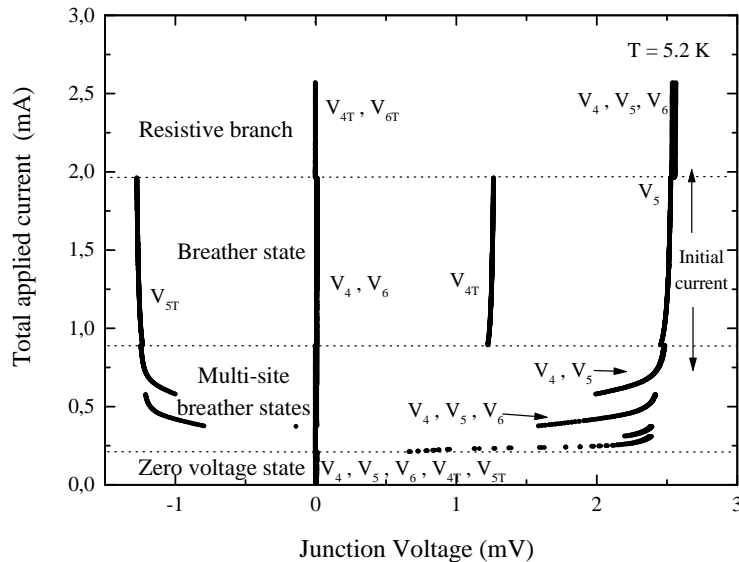


Fig. 26. Measured time-averaged voltages of five junction in the center of the array as the applied current is varied. V_4, V_5, V_6 stand for the voltage in vertical junctions number 4,5 and 6 in a 9 junction ladder. V_{4T} and V_{5T} for horizontal junctions in the top branches connecting the three previously mentioned vertical junctions. The breather state was excited at a current close to 1.4mA. When the current was increased the breather solution became unstable at a current close to 2mA and the array switches to a uniform resistive state, where all the vertical junction rotate with a same voltage. We can see that for the breather state $V_4 = V_6 = 0$ and $V_{4T} = -V_{5T} = V_5/2$ which corresponds to the breather state that we have coined as type-B state. In a second experiment, a new breather was excited but now the current was decreased. We observed that the breather becomes unstable at a current close to 0.8mA and a new breather state is excited. This is a multi-site breather state. New instabilities between different multi-site states occur and finally the array reaches its zero-voltage state at about 0.2mA.

A and type-B (Fig. 23) breather solution. It can be seen that, as expected, the flux decays exponentially.

Figure 25 shows a picture of one of the anisotropic arrays where DB were excited and detected.^{55,62,40} It is a ladder array with nine vertical junctions biased by an external current source. The array was designed with voltage probes in different vertical junctions (junction 4,5,6, and 9) to measure local voltage at different points of the array (we can measure for instance $V_4, V_5, V_6, V_9, V_{4T}, V_{5T}$ and any other combination of the terminals). Sometimes, when we swept the applied current we found that DB solutions appear spontaneously. However for the experiments, we developed a simple

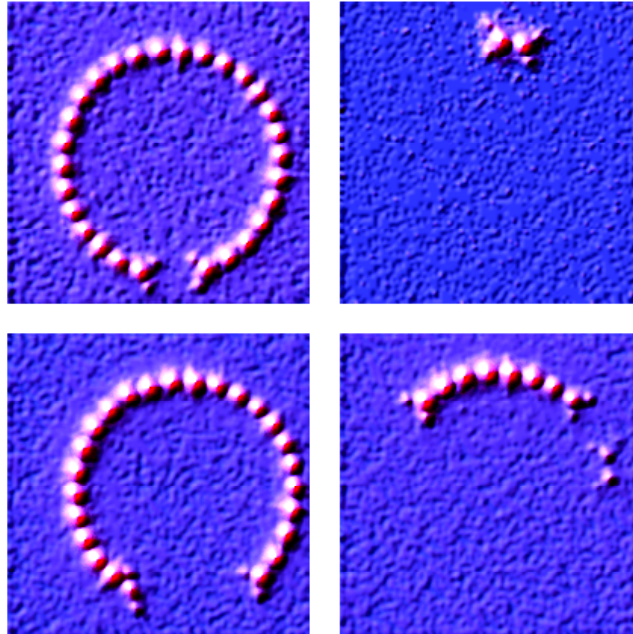


Fig. 27. LTSM image of four different multi-site breather states in an annular Josephson ladder array. Figure from <http://www.pi3.physik.uni-erlangen.de/ustinov/>.

reproducible method of exciting a breather: (i) Bias the array uniformly to a current below depinning current; (ii) increase the current injected into the middle vertical junction (V_5) until its voltage switches to the gap; (iii) reduce this extra current in the middle junction to zero. Other procedures are also possible.

Fig. 26 shows the result after we have excited the breather and we have increased or decreased the array current. The breather was excited at $I_a \approx 1.4$ mA and then the junction voltages were measured as the applied current was increased or decreased. The DB is initially in the fifth vertical junction ($V_4=V_6=0$ and $V_5 \neq 0$). When increasing the external current, the breather exists until a maximum current where all the junctions switch to the gap. When decreasing the external current different scenarios were found but typically the breather enlarges from one-site to multi-site breather solutions and then at small enough current the array decays to

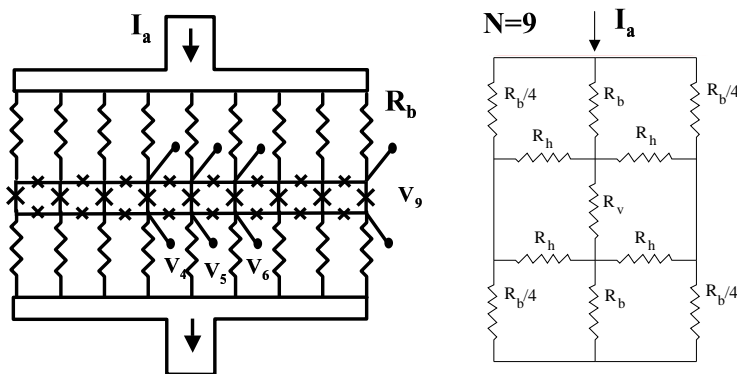


Fig. 28. Ladder array biased by an external current and equivalent circuit for the dc model of a one-site type-B breather.

the uniform superconducting state. More details about the experiment can be found in Ref. 62

Figure 27 shows a low temperature scanning microscopy image of an annular ladder with different multi-site breather solutions. Such pictures were obtained by the group of Alexey Ustinov at Erlangen³⁹. The experimental results confirmed the existence of many different breather states in open and annular ladders. In the figure we can observe breathers where two vertical junction are rotating and large multi-site breather states where most of the vertical junctions rotate.

5.4.1. Analysis of the breather solutions using a dc model

The simplest theoretical approach to the study of the dynamics of breathers in Josephson arrays is the use of a dc model for the circuit. In this model rotating vertical junctions have a resistance of R_v and rotating horizontal junctions have a resistance of R_h . Oscillating junction will be modeled as shorts. Then we reduce the array to a simple network of resistors and calculate DC properties. The equivalent resistor network for a single-site symmetric breather (type-B breather) located on junction 5 in our 9 junction array is shown in Fig. 28. In addition to its simplicity this model allows to include the effect of the bias resistors (used to distribute uniformly the current through the array).

We will also make the following assumptions: $V_v = sV_h$, $R_v = hR_h$; where $s=1$ for type-A solutions and $s=2$ for type-B solutions and h is the

parameter which describes the anisotropy of the array.

Using this model we make the following predictions for type-A ($s=1$) or type-B ($s=2$) m -site breathers.⁶² We present here results for large bias resistances $R_b \gg R_h$ (uniform driving condition).

- The IV curve is given by

$$I_a/N = (1 + 2h/sm)V_v/R_v \quad (49)$$

- The minimum current for the breather solution I_{min} (defined from junction retrapping) is given by

$$i_{min} = I_{min}/NI_{cv} = (2h/m + s)(4/\pi)\Gamma \quad (50)$$

- The maximum current for the breather solution I_{max} (defined from junction switching) is given by

$$i_{max} = I_{max}/NI_{cv} = (2h + sm)/[(2 + m)h + sm] \quad (51)$$

- The effect of the bias resistors in the current distribution is

$$I_5 = [1 + mh/(2h + sm)(1 - m/N)R_h/R_b]^{-1}(I_a/N) \quad (52)$$

For $N=9$, $m=1$, $s=2$, $R_h/R_b \sim 0.8$ and $h=0.25$, we have $I_5 = 0.934I_a/N$ and $I_j = 1.008I_a/N$ ($j \neq 5$).

Figure 29 shows a comparison of the theoretical predictions obtained from the dc model with the experimental results. The different values of Γ in the figure correspond with experiments done at different temperatures from 4.2 to 6.7 K

Although the analysis based on the dc model has been found to be helpful, it presents some important limitations: The model can not account for any λ dependence. It can not explain resonances between breather dynamics and normal modes of the ladder. Such resonances can drive the breather to destabilize. The model allows for an estimation of parameter values where the breather solution ceases to exist but it gives no information on the dynamical state after the destabilization of the localized solution.

5.4.2. Simulations

The breather dynamics has been extensively studied by numerical integration of the Eqs. (47) using an standard 4th order RK scheme. Such integrations are complemented with Floquet stability analysis^{64,65} of periodic solutions and the study of the robustness of the breather solutions against

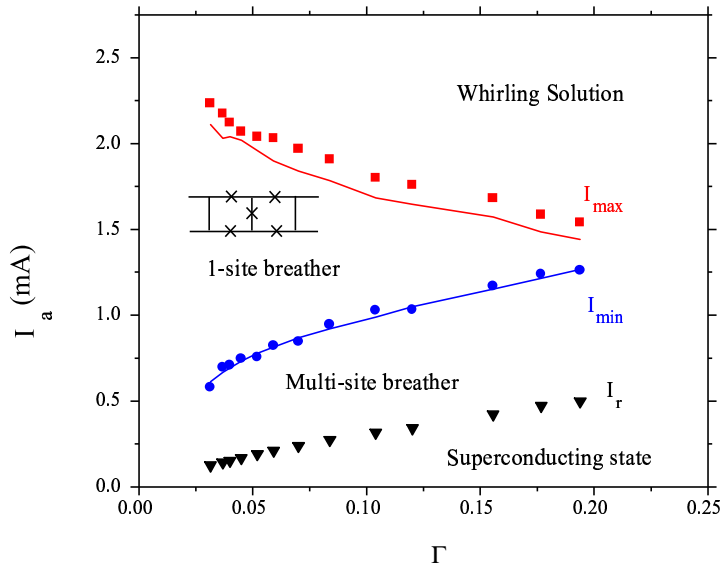


Fig. 29. Comparison between results based on the dc model and experimental results.

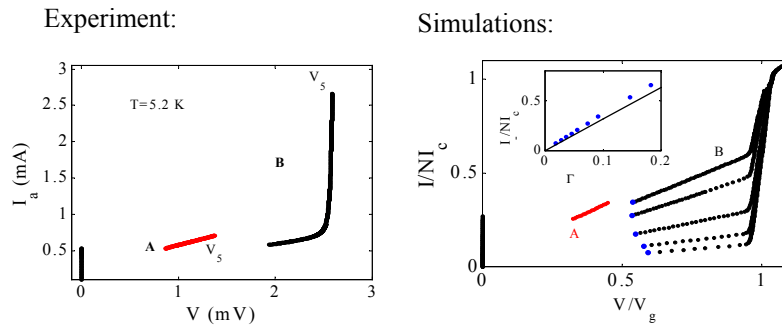


Fig. 30. Experiment (left) and simulation (right) of a type-B breather. The simulations have been done considering different subgap resistances. The experiment, and one of the simulations (upper curve), when decreasing the current show that the type-B breather destabilizes to a type-A one.

thermal fluctuations, modeled by including a noise term in the junction current (see Eq. (8)).

In addition to the noise, in order to get a more detailed description of

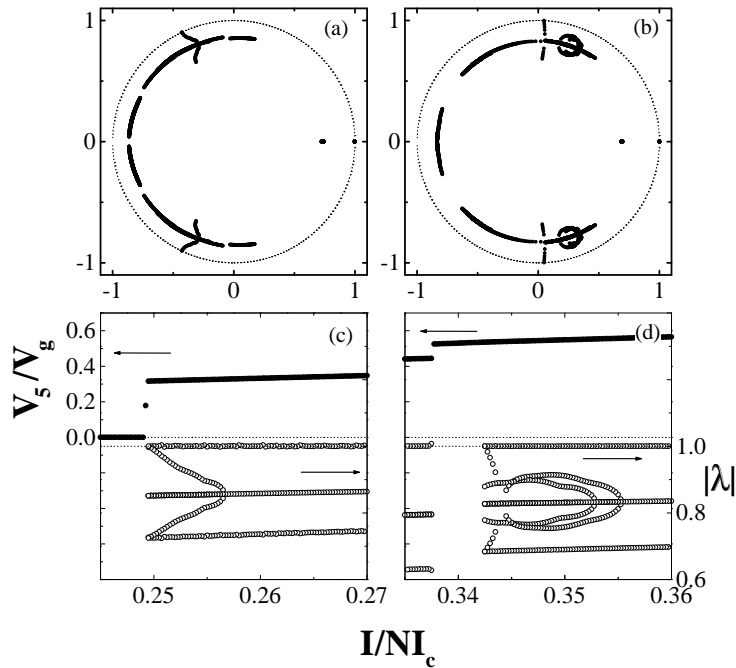


Fig. 31. Floquet multipliers of the type-A (a) and type-B (b) periodic DB showed in Fig. 30 (upper simulation). Figures (c) and (d) show as a function of the current the value of voltage (solid circles) and the modulus of the Floquet multipliers whenever the solution is periodic (open circles).

the system, the model defined in Eqs. (47) can be extended to take into account the nonlinear character of the junction resistance or to include the bias circuit. We usually work at zero external field, however the model allows for the inclusion of other external magnetic fields. Finally, we can also study the effect of considering the full-inductance matrix of the circuit and incorporate disorder, randomizing the junctions critical currents.

In this section we will present simulations made at $\Gamma \simeq 0.1$, $h \simeq 0.25$ and $\lambda \simeq 0.05$. Such values of the parameters are close to the expected parameter values for the experiments reported above.

Figure 30 shows an experimental IV curve of a breather solution that decreasing the current destabilizes from a 1-site type-B solution to a 1-site type-A one. The figure also shows the result of a simulations done including in the model the subgap resistance (as explained in Sec. 2.1) and

for different values of this subgap resistance.

Figure 31 shows numerically computed Floquet multipliers for the simulation presented in the previous figure. Fig. 31(b) shows the distribution of the Floquet multipliers at several values of the applied current close to the destabilization current for the type-B breather. Fig. 31(d) shows the voltage and the modulus of the Floquet multipliers (only for periodic solutions) when we decrease the current. This is the typically observed bifurcation scenario for small λ . It seems that for small λ and underdamped junctions, this instability introduces more frequencies in the solution. When the periodic type-B breather loses stability the solution becomes a quasi-periodic type-B breather. This quasi-periodic type-B solution persists up to a smaller current when the array jumps to a periodic type-A solution. For large λ , however, we usually observe a period-doubling bifurcation where a multiplier crosses the unit circle at -1 , though the behavior also depends on the damping.

Fig. 31(a) shows the Floquet multipliers for a type-A breather at different current values. In Fig. 31(c) we decrease the current and show the value of the voltage and the modulus of the Floquet multipliers. Below $I \sim 0.25$ the periodic breather is unstable and the solution switches to the superconducting state.

5.4.3. Breather existence diagrams

Now we are going to show a series of figures with breather existence diagrams calculated from the results of the dc model and computed with a numerical integration of the system equations.

The equations found in Sec. 5.4.1 allow for a calculation of the IV curves and the maximum and minimum values of external currents supporting DBs. If we write the equations for the single-breather state and use normalized parameters we find

$$\begin{aligned} i &= (1 + 2h/s)\Gamma v_v, \\ i_- &= (2h + s)4\Gamma/\pi, \\ i_+ &= (2h + s)/(3h + s), \end{aligned} \tag{53}$$

where currents are normalized by NI_{cv} and $v_v = \langle \dot{\phi}_v \rangle$.

Figs. 32 and 33 show the predictions given by the circuit model. The size of the existence regions decreases rapidly when the damping or the anisotropy increase. On the other hand, if the damping is small enough the equations predict the existence of localized solutions even at large values of

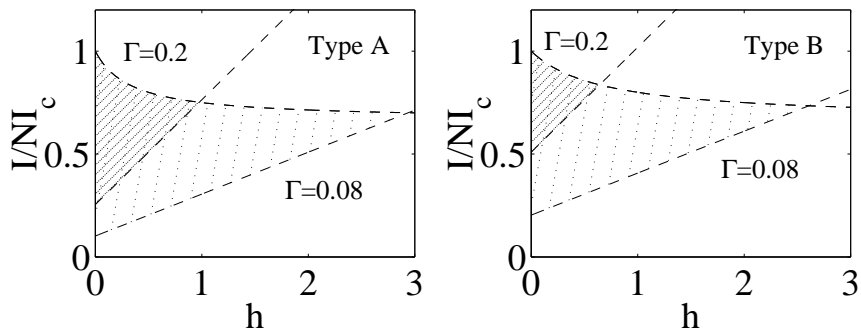


Fig. 32. Prediction of Eqs. (53) for i_+ and i_- as a function of h for single-site type-A (left) and type-B (right) solutions and two values of the damping. Lightly hatched region corresponds to $\Gamma = 0.08$ and the densely one to $\Gamma = 0.2$

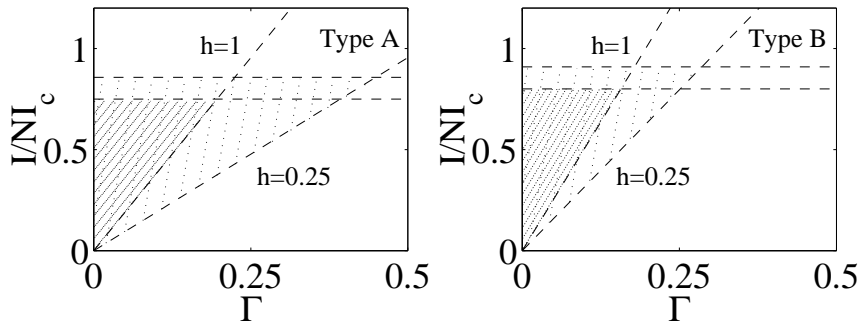


Fig. 33. Prediction of Eqs. (53) for i_+ and i_- as a function of Γ for single-site type-A (left) and type-B (right) solutions and two values of the anisotropy. Lightly hatched region corresponds to $h = 0.25$ and the densely one to $h = 1.0$

h . We also see that the existence regions are larger for type-A solutions.

This simple model, however, does not account for any dependence of the curves with the parameter λ . This is an important limitation of the dc model and we have confirmed in the numerical simulations that λ affects our predictions in two important ways. First, it affects the value of the array retrapping current. The value used in our circuit models has been calculated from a single junction and should be corrected by λ in the case of the array. Second, it governs the values of the voltage at which resonances between the breather and the normal modes of the array play an important role. Roughly speaking, the resonances split the diagrams in three different

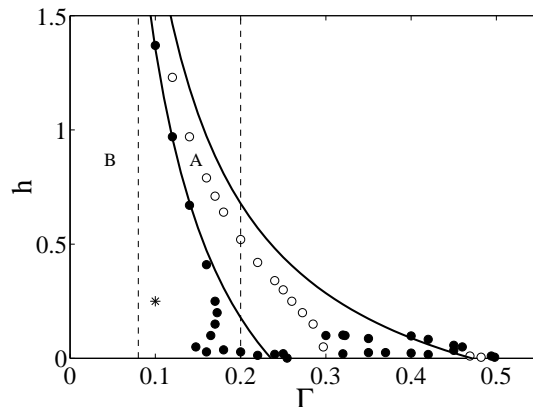


Fig. 34. Numerical calculation of the existence region of single-site DBs when $\lambda = 0.04$ and $I = 0.6$. Open circles correspond to type-A and solid circles to type-B solutions. Vertical lines correspond to cuts show in Fig. 36 and the asterisk to the experiments.

regions: The small, the moderate and the large λ regions. When λ is small, the resonance frequency is smaller than the breather frequency, and when λ is large the resonance frequency is larger. Thereby, complications of damped resonances between the DB and the lattice eigenmodes are avoided in these limits

Far from the resonance values the effect of λ is a small correction to our IV curves. This is shown by the numerical simulations. See for instance Figs. 37 and 41, where can be seen that the IV curves numerically integrated agree quite well with the predictions of the dc model.

We have also done numerical simulations based on Eqs. (47) with $f_0 = 0$ in order to study the λ dependence of the breather existence region. The results are presented in Figs. 34, 35, and 36. In these diagrams we show the maximum and minimum values of the parameters for which a localized solution has been numerically found. In some cases the characterization of the solutions inside the existence regions is quite complex and several resonances and transitions between periodic and aperiodic localized states appear.

Figure 34 shows the existence regions in the anisotropy versus damping plane when $\lambda = 0.04$ and $I = 0.6$. The figure confirms that DBs exist at large values of h if Γ is small enough. Fig. 35 shows the existence regions in the current versus λ plane when $\Gamma = 0.08$ and $h = 0.25$. These are the estimated values of h and Γ in our experiments. Fig. 36 shows the diagram

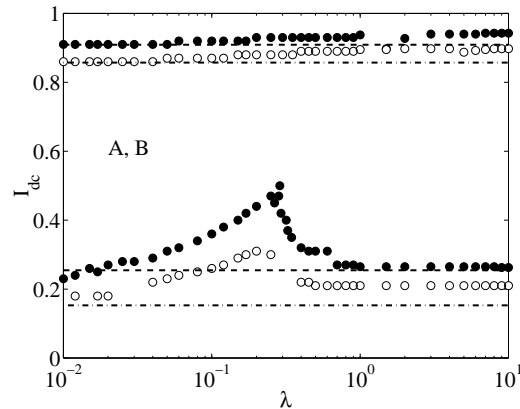


Fig. 35. Numerical calculation of the existence region of single-site DB when $\Gamma = 0.08$ and $h = 0.25$. Open circles correspond to type-A and solid circles to type-B solutions. Horizontal lines correspond to the predictions of the circuit model.

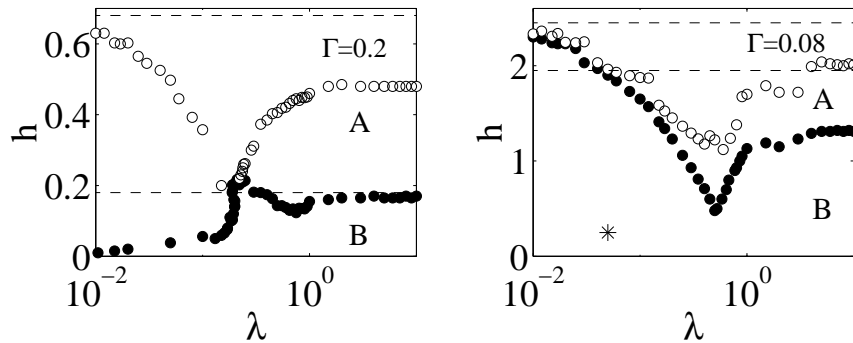


Fig. 36. Numerical calculation of the existence region of single-site DB when $I = 0.6$ and $\Gamma = 0.2$ (left) and $\Gamma = 0.08$ (right). Open circles correspond to type-A and solid circles to type-B solutions. Horizontal lines correspond to the predictions of the circuit model and the asterisk to the experiments.

in the anisotropy versus λ plane for $I = 0.6$ and $\Gamma = 0.2$ (left) and 0.08 (right). The asterisk in the $\Gamma = 0.08$ figure approximately corresponds to the value of the parameter where our experiments were done. We can see in the figures that at moderate λ there is a substantial deviation from the predictions of the dc model. This deviation is caused resonances and other dynamical effects.

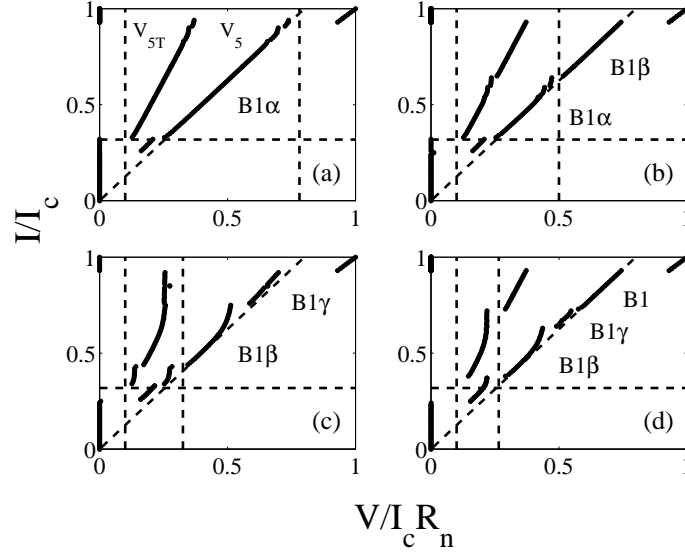


Fig. 37. Simulated IV's for 9×1 ladder of type-B breather as a function of λ . $h = 0.25$, $\Gamma = 0.1$, $f = 0$ and (a) $\lambda = 5$, (b) $\lambda = 2$, (c) $\lambda = 0.8$, and (d) $\lambda = 0.5$. The labels indicate different type-B breather solutions. The vertical dashed lines are $\omega_+(\lambda)$ and $\omega_- = 1$ from Eq. 54. The horizontal dashed line is I_- and the diagonal dashed line is the IV curve, both from Eq. 53.

5.4.4. Different λ regimes

In order to understand the role of λ in the simulations we need to study the basic linearized excitations that can occur. Complex behavior appears when the frequency of the rotating junction resonates with the ladder eigenmodes. To calculate the resonant frequencies, we linearize Eq. (47) around a solution. The linear analysis allows to compute such frequencies and the decay length.^{62,66,59} The dispersion relation has two branches defined by

$$\begin{aligned}\omega_+ &= \sqrt{1 + \frac{2\lambda}{h} + 4\lambda \sin^2 \frac{q}{2}} \\ \omega_- &= 1,\end{aligned}\tag{54}$$

and we can also estimate the decay length for our waves,

$$\zeta = \cosh^{-1} \left| \frac{2\lambda(h+1) + h}{2\lambda h} - \frac{\omega^2}{2\lambda} \right|.\tag{55}$$

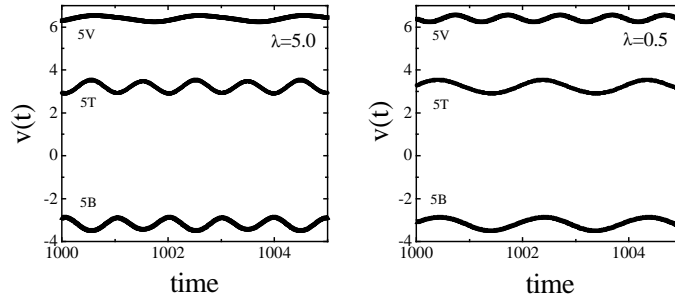


Fig. 38. Time evolution of the time derivative of the phase, $v(t) = d\varphi/dt$, for the large λ type-B solution labeled B1 α in Fig. 37(a) and the small λ type-B solution depicted as B1 in Fig. 37(d). We plot $v(t)$ for the rotating vertical junction (5V) and two neighbor horizontal junctions (5T and 5B). Here, $h = 0.25$, $\Gamma = 0.1$ and $I = 0.8$.

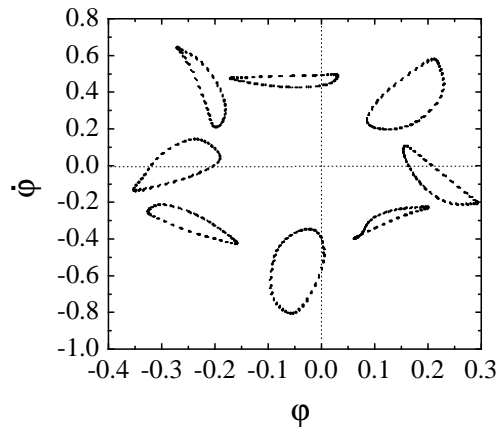


Fig. 39. Poincaré sections of the third top junction (3T) for a B1 γ solution. The phases are shown at times $t = t_0 + n\tau$ where $\tau = 2\pi/V_5$ and $h = 0.25$, $\Gamma = 0.1$, $\lambda = 0.5$, and $I = 0.7$.

Equation (54) defines three physical regimes in the system:

- (i) $\omega > \omega_R$ (small λ)
- (ii) $\omega \sim \omega_R$ (moderate λ)
- (iii) $\omega < \omega_R$ (large λ)

The existence of such regimes has been confirmed by the numerical simu-

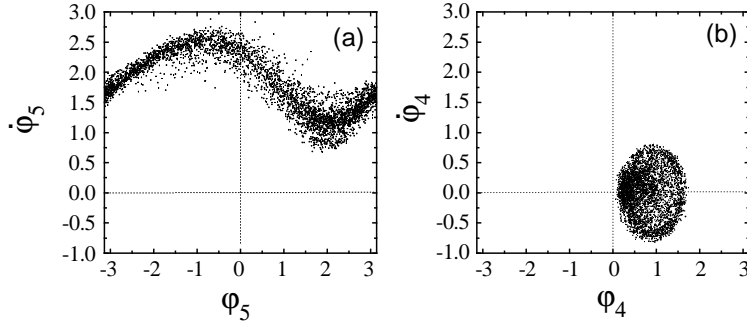


Fig. 40. Poincaré sections of the fourth and fifth vertical junctions for a type-B chaotic solution. The phases are shown at times $t = t_0 + n\tau$ where $\tau = 2\pi/V_5$ and $h = 0.15$, $\Gamma = 0.2$ and $\lambda = 0.2$ and $I = 0.6$. (a) Shows the sections for the rotating vertical junction 5 and (b) for its first neighbor, 4.

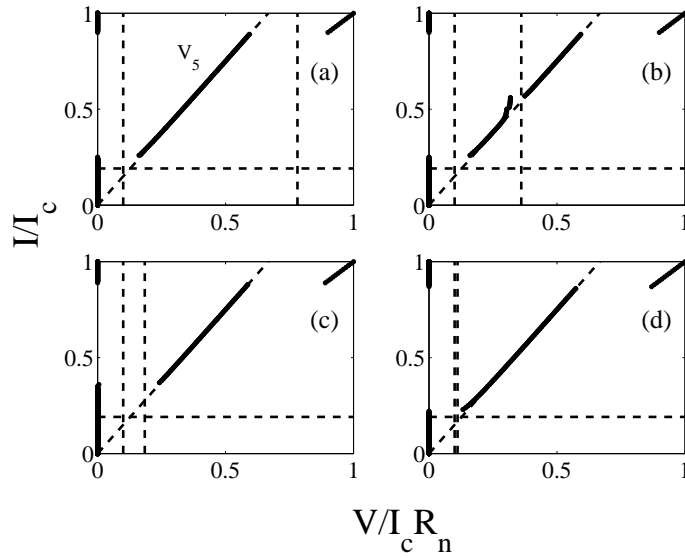


Fig. 41. Simulated IV's for 9×1 ladder of type-A breather as a function of λ . Here, $\Gamma = 0.1$, $f = 0$ and (a) $\lambda = 5$, (b) $\lambda = 1$, (c) $\lambda = 0.2$, and (d) $\lambda = 0.02$. The vertical dashed lines are $\omega_+(\lambda)$ and $\omega_- = 1$ from Eq. (54). The horizontal dashed line is I_- and the diagonal dashed line is the IV curve, both from Eq. (53).

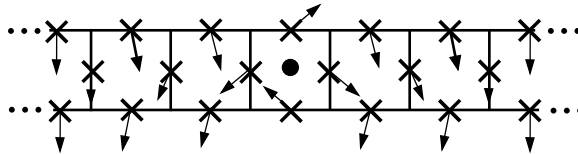


Fig. 42. A vortex configuration in the ladder ($I = 0$). Arrows represent phase differences. The phases of the vertical junctions change from 0 to 2π as we move from one edge to other of the ladder.

lation of IV curves at different values of λ .

Figure 37 shows IV curves at different values of λ of a ladder with a type-B breather ($h=0.25$, $\Gamma=0.1$). From (a) to (d), $\lambda = 5, 2, 0.8, 0.5$. Labels indicate different types of solutions. Dashed lines are voltage resonances and prediction for I_{min} . We have observed that for large λ the solution is up-down symmetric (see Fig. 38 at $\lambda = 5.0$). However, at small values of λ top and bottom junctions show a dephase of half period (Fig. 38 at $\lambda = 0.5$). Intermediate values of λ show more complex solutions: for instance quasiperiodic (Fig. 39) and chaotic (Fig. 40) solutions. Stable resonant breather solutions appear at moderate values of λ . Such solutions have been also experimentally observed.⁶⁷

Figure 41 shows IV curves at different values of λ of a ladder with a type-A breather ($h=0.25$, $\Gamma=0.1$). From (a) to (d), $\lambda = 5, 1, 0.2, 0.02$. Dashed lines are voltage resonances and prediction for I_{min} . Again, we can see the existence of resonant breather solutions at intermediate values of λ .

5.4.5. Breather-vortex collision in the Josephson ladder

In the same way that kinks exist in parallel arrays and vortices in 2D arrays, the nonlinear static excitations in the ladder are called vortices.

The static properties of a vortex in the ladder are in many aspects similar to those of a kink in the Frenkel-Kontorova or discrete sine-Gordon system.⁶⁸⁻⁷⁰ There are however some differences, the most important of which is the existence of a critical magnetic field $f_c(\lambda)$ for which if $f < f_c$ a single vortex is not stable in the ladder. Below this critical field the vortex is expelled from the ladder through the horizontal junctions. Thus, vortices are stable static solutions of the array at adequate parameter values. In the absence of external currents, a static vortex in the ladder correspond to a solution for which the phase of the vertical junctions φ_j^v go from 0 to 2π (see Fig. 42).

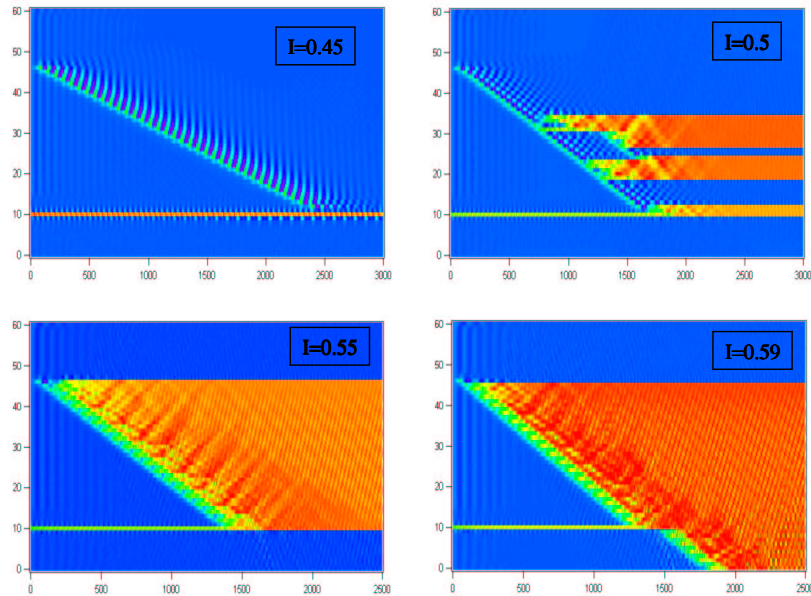


Fig. 43. Simulations a vortex-breather collisions in a Josephson ladder.⁷¹ For all the cases the initial condition is a 1-site rotobreather in junction 11 of the ladder and a vortex in junction 47. The figures plot the value of the instantaneous voltage at every vertical junction.

We have studied vortex-breather collision in a Josephson-junction ladder array.⁷¹ We have computed parameters values of the system for which both types of structures coexist in the ladder. Then, by increasing the circuit bias current, we have found different possible scenarios for vortex-breather collisions (Fig. 43). (i) The breather acts as a pinning center for a single vortex. (ii) Increasing the current, the vortex excites multi-site breathers on its way and is finally pinned by the breather. (iii) Now a whirling mode front is excited by the vortex. However the breather still acts as a pinning center, now for the front. (iv) At higher values of the bias, the front is able to destroy the breather.

For scenario (i), we have also studied thermal activation properties associated with the presence of the vortex-breather pair in the array. We have seen that noise causes the depinning of the vortex and the breather decays into a 2-site breather. The escape time for this process showed an exponential dependence in temperature with an activation energy of 22K.

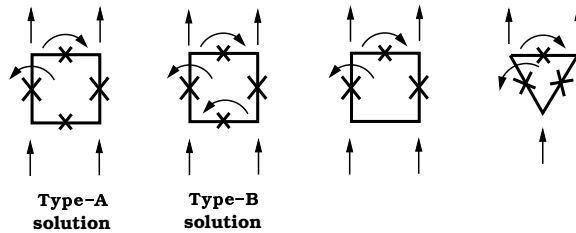


Fig. 44. Sketches of generalized breather solutions in single cell arrays with four and three Josephson junctions.

5.5. Single-plaquette arrays

Rotobreather-like solutions can be also studied in single-plaquette arrays. Fig. 44 sketches such solutions in cell arrays with three or four JJs. The case of a square cell with four JJs was considered in Refs. 60 and 62. In this case the breather can be seen as a reduction of the solutions found in the ladder when we impose mirror symmetry with respect to the rotating junction and neglect the dynamics of junctions beyond the first neighbor of the rotating ones. Doing so, we are left with a square plaquette with four junctions. The equations for the ladder can be mapped onto the equations of the plaquette with $h_{\text{plaq.}} = 2h_{\text{ladd.}}$ and $\lambda_{\text{plaq.}} = 2\lambda_{\text{ladd.}}$. Then it was found that many of the main aspects concerning DB solutions in the ladder can be studied in single cell arrays.

The analytical and numerical study of the rotobreather states in a single plaquette with three junctions^{72,73} showed that this system is complex enough to present most of the phenomena observed in Josephson ladders. The experimental study of the array⁷⁴ confirmed the theoretical and numerical results.

5.6. DBs in two-dimensional Josephson junction arrays

Two-dimensional Josephson-junction arrays have already been studied in Sec. 4.1 in the context of vortices. Here we are going to present numerical results on the existence of rotobreathers in such arrays.⁷⁵

Based on theoretical arguments from the uncoupled limit of the lattice and on numerical simulations, rotobreather solutions have been predicted to exist in 2DJJA biased by ac currents. The rotobreathers in 2D arrays correspond to voltage localized solutions sketched in Fig. 45. There, four junctions sited in the bulk of the array are in the resistive state, two with voltages $+V$ and two with $-V$, while the rest follow the ac field in a oscil-

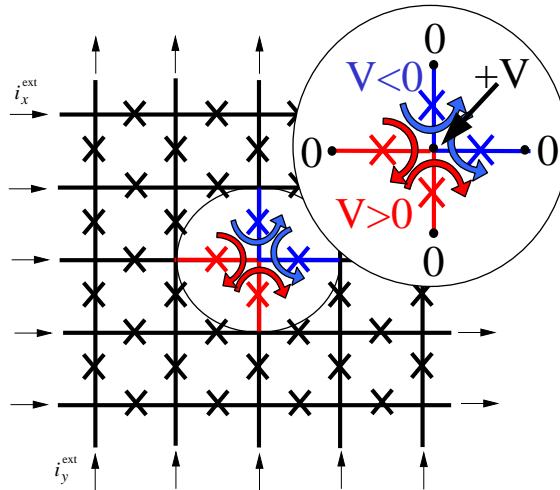


Fig. 45. Sketch of the 2DJJA with breather

lating state of mean voltage $V = 0$. From the pictures of the dynamics of a single junction (Fig. 21) we see that such scenario of coexistence of three different attractors (0 , $+V$, and $-V$) is only possible under ac bias [Figs. 21(c) and (d)]. Thus in the case of 2D arrays we will study rotobreather solutions biased by ac fields.

It can be seen that uncoupled limits can be obtained when $\lambda \rightarrow 0$ or when $h \rightarrow 0$ in the array (Eqs. (29) and (30)). In any of these limits the junctions behave as independent oscillators where -trivial- localized solutions can be obtained when the array is biased by ac external fields $i_{\text{ext}} = i_{ac} \sin \omega t$.

We have been able to excite and study DBs in many different regions of the parameter space and under diagonal or vertical bias. We have tried large and small values of λ , large and small values of h , different values of the frequency, damping, field amplitude, different array sizes,...

Figure 46 shows four snapshots along one period of the phase dynamics for two rotobreather solutions simulated in two very different situations (see caption).

In addition to the numerical integration of Eqs. (29) we have found that the obtained breather solutions are linearly stable in the framework of the Floquet stability theory and persist in the presence of thermal fluctuations (current noise). We also checked that the solutions also exist when applying

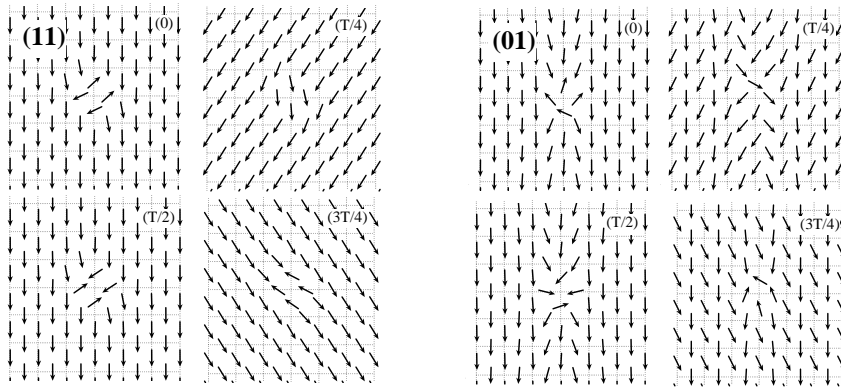


Fig. 46. Four snapshots of the phase evolution for two different DB solutions in a 2DJJA with different bias and very different parameter values. Arrows represent phases of the junctions and we show the central part of a 11×11 array. The solutions are time periodic (period T) and time increases from 0 (arbitrary) to $3T/4$ as labeled. The rotobreather solution is localized in the four central junctions which rotate. Left: current is biased in the diagonal or (11) direction ($\lambda = 0.1$, $h = 1.0$, $i_{ac} = 5.0$, $\Gamma = 0.003$ and $\omega = \pi$). Right: current is biased along the y or (01) direction ($\lambda = 5.0$, $h = 0.05$, $i_{ac} = 0.7$, $\Gamma = 0.02$ and $\omega = \pi/2$).

an external magnetic field and studied the mechanisms involved in the destabilization of the localized solution when changing some of the system parameters.

In relation to the issue of a possible experimental observation of DB's in 2DJJA, the simulations were done at experimentally accessible parameter values and it was found a numerical protocol to excite DB's in the array. The protocol is based in the possibility of adding a local dc current that should be injected in one central island of the array and extracted from the four neighboring islands. With respect to a detection, it can be done for instance by measuring local voltages in different points of the array.

To finish we want to mention that we have also studied and obtained rotobreather solutions in the dynamics of the array in the infinite λ (no induced magnetic flux) limit.⁷⁶ In this limit the equations correspond to a realization of the dynamics of the two-dimensional XY model.

Acknowledgments

This lecture is the result of years of work in collaboration with many people. Special thanks are given to F. Falo, L. M. Floría and T. P. Orlando for their guide and collaboration and hospitality. I acknowledge P. J. Martínez and

E. Trías for many collaborations and discussions in these topics. Thanks to M. V. Fistul, S. Flach, J. L. García-Palacios, J. L. Marín, F. Pignatelli, M. Schuster, K. Segall and A. V. Ustinov for insightful discussions. Financial support is acknowledged to FEDER program through BFM2002-00113 project and European Network LOCNET HPRN-CT-1999-0016.

References

1. See for instance the book by A. Scott, *Nonlinear Science: Emergence & Dynamics of Coherent Structures*. Oxford University Press, 1999.
2. B. D. Josephson, "Possible new effect in superconductive tunneling". *Phys. Lett.* **1**, 251-253 (1962).
3. J. R. Waldram, "The Josephson effect in weakly coupled superconductors". *Rep. Prog. Phys.* **39**, 751-821 (1976).
4. A. Barone and G. Paternò, *Physics and applications of the Josephson effect*. John Wiley, 1982.
5. K. K. Likharev, *Dynamics of Josephson junctions and circuits*. Gordon and Breach Science, 1984.
6. T. P. Orlando and K. A. Delin, *Foundations of applied superconductivity*. Addison Wesley, 1991.
7. M. Tinkham, *Introduction to superconductivity*. Mc Graw Hill, 1996.
8. A. Barone, "Weakly coupled macroscopic quantum systems: likeness with difference". In *Quantum Mesoscopic Phenomena and Mesoscopic Devices in Microelectronics*, pp. 301-320. Edited by I. O. Kulik, Kluwer Academic, 2000.
9. O. Avenel and E. Varoquax, "Josephson effect and quantum phase slippage in superfluids". *Phys. Rev. Lett.* **60**, 416-419 (1988).
10. A. J. Leggett "Bose-Einstein condensation in the alkali gases: some fundamental concepts". *Rev. Mod. Phys.* **73**, 307-356 (2001).
11. V. Ambegaokar and A. Baratoff, "Tunneling between superconductors". *Phys. Rev. Lett.* **10**, 486-489 (1963) and erratum **11**, 104 (1963).
12. W. C. Stewart, "Current-voltage characteristics of Josephson junctions". *Appl. Phys. Lett.* **12**, 277-280 (1968).
13. D. E. McCumber, "Effect of ac impedance on dc voltage-current characteristics of superconductor weak-link junctions". *J. Appl. Phys.* **39**, 3113-3118 (1968)
14. T. Van Duzer and C. W. Turner, *Principles of Superconductive Devices and Circuits*. Pearson Education POD, 1998.
15. P. Hänggi, P. Talkner and M. Borkovec, "Reaction-rate theory: fifty years after Kramers". *Rev. Mod. Phys.* **62**, 251-341 (1990)
16. V. I. Mel'nikov, "The Kramers problem: fifty years of development". *Phys. Rep.* **209**, 1-71 (1991)
17. A. V. Ustinov, "Solitons in Josephson junctions". *Physica D* **123**, 315-329 (1998).
18. J. Clarke, A. N. Cleland, M. H. Devoret, D. Esteve and J. M. Martinis,

- “Quantum mechanics of a macroscopic variable: the phase difference of a Josephson junction”. *Science* **239**, 992-997 (1988).
19. L. J. Geerlings, V. F. Anderegg, J. Romijn and J. E. Mooij, “Single Copper-pair tunneling”. *Phys. Rev. Lett.* **65**, 377-380 (1990).
 20. W. J. Elion, M. Matters, U. Geigenmüller and J. E. Mooij, “Demonstration of Heisenberg’s uncertainty principle in a superconductor”. *Nature* **371**, 594-595 (1994).
 21. Penttilä, Ü. Parts, P. J. Hakonen, M. A. Paalanen and E. B. Sonin, “Superconductor-Insulator Transition in a Single Josephson Junction”. *Phys. Rev. Lett.* **82**, 1004-1007 (1999).
 22. A. Wallraff, A. Lukashenko, J. Lisenfeld, A. Kemp, M. V. Fistul, Y. Koval, and A. V. Ustinov, “Quantum dynamics of a single vortex”. *Nature* **425**, 155-158 (2003).
 23. Y. Nakamura, Yu. A. Pashkin and J. S. Tsai, “Coherent control of macroscopic quantum states in a single-Cooper-pair box”. *Nature* **398**, 786-788 (1999).
 24. J. R. Friedman, V. Patel, W. Chen, S. K. Tolpygo and J. E. Lukens, “Quantum superposition of distinct macroscopic states”. *Nature* **406**, 43-46 (2000).
 25. C. H. Van der Waal, A. C. J. ter Haar, F. K. Wilhelm, R. N. Schouten, C. J. P. M. Harmans, T. P. Orlando, S. Lloyd and J. E. Mooij, “Quantum superposition of macroscopic persistent-current states”. *Science* **290**, 773-777 (2000).
 26. D. Vion, A. Aassime, A. Cottet, P. Joyez, H. Pothier, C. Urbina, D. Esteve and M. H. Devoret, “Manipulating the quantum state of an electrical circuit”. *Science* **296**, 886-889 (2002).
 27. Y. Yu, S. Han, X. Chu, S. Chu and Z. Wang, “Coherent temporal oscillations of macroscopic quantum states in a Josephson junction”. *Science* **296**, 889-892 (2002).
 28. I. Chiorescu, Y. Nakamura, C. J. P. M. Harmans and J. E. Mooij, “Coherent quantum dynamics of a superconducting flux qubit”. *Science* **299**, 1869-1871 (2003).
 29. Yu. A. Pashkin, T. Yamamoto, O. Astafiev, Y. Nakamura, D. V. Averin and J. S. Tsai, “Quantum oscillations in two coupled charge qubits”. *Nature* **421**, 823-826 (2003).
 30. C. A. Hamilton, C. J. Burroughs and S. P. Benz, “Josephson voltage standard: A review”. *IEEE Trans. Appl. Supercond.* **7**, 3756-3761 (1997).
 31. J. Clarke, “Principles and applications of SQUIDs”. *Proc. IEEE* **77**, 1208-1223 (1989).
 32. S. T. Ruggiero and D. A. Rudman (eds.), *Superconducting Devices*. Academic Press, 1990.
 33. D. Koelle, R. Kleiner, F. Ludwig, E. Dantsker and J. Clarke, “High-transition-temperature superconducting quantum interference devices”. *Rev. Mod. Phys.* **71**, 631-686 (1999).
 34. L. M. Floría and J. J. Mazo, “Dissipative dynamics of the Frenkel-Kontorova model”. *Adv. Phys.* **45**, 505-598 (1996).
 35. O. Braun and Y. Kivshar, “Nonlinear dynamics of the Frenkel-Kontorova

- model". *Phys. Rep.* **306**, 1-108 (1998).
36. O. Braun and Y. Kivshar, *The Frenkel-Kontorova model. Concepts, methods and applications*. To be published by Springer.
 37. A. V. Ustinov, M. Cirillo and B. A. Malomed, "Fluxon dynamics in one-dimensional Josephson-junction arrays". *Phys. Rev. B* **47**, 8357-8360 (1993).
 38. S. Watanabe, H. S. J. van der Zant, S. H. Strogatz and T. P. Orlando, "Dynamics of circular arrays of Josephson junctions and the discrete sine-Gordon equation". *Physica D* **97**, 429-470 (1996).
 39. A. V. Ustinov, "Imaging of discrete breathers". *Chaos*, **13**, 716-724 (2003).
 40. J. J. Mazo and T. P. Orlando, "Discrete breathers in Josephson arrays", *Chaos*, **13**, 733-743 (2003).
 41. R. S. Newrock, C. J. Lobb, U. Geigenmüller and M. Octavio, "The two-dimensional physics of Josephson-junction arrays". *Sol. State Phys.* **54**, 263-512 (2000).
 42. P. Hadley, M. R. Beasley and K. Wiesenfeld, "Phase-locking of Josephson-junction series arrays". *Phys. Rev. B* **38**, 8712-8719 (1988).
 43. H. J. Mooij and G. Schön, "Single charges in 2-dimensional junction arrays". In *Single Charge Tunneling*, pp. 275-310. Ed. by H. Grabert and M. H. Devoret, Plenum Press, 1992.
 44. R. Fazio and H. S. J. van der Zant, "Quantum phase transitions and vortex dynamics in superconducting networks". *Phys. Rep.* **355**, 235-334 (2001).
 45. P. Delsing, "One-dimensional arrays of small tunnel junctions". In *Single Charge Tunneling*, pp. 249-274. Ed. by H. Grabert and M. H. Devoret, Plenum Press, 1992.
 46. D. B. Haviland and P. Delsing, "Cooper-pair charge solitons: the electrodynamic of localized charge in a superconductor". *Phys. Rev. B* **54**, R6857-R6860 (1996).
 47. F. Falo, P. J. Martínez, J. J. Mazo and S. Cilla, "Ratchet potential for fluxons in Josephson-junction arrays". *Europhys. Lett.* **45**, 700-706 (1999).
 48. E. Trías, J. J. Mazo, F. Falo and T. P. Orlando, "Depinning of kinks in a Josephson-junction ratchet array". *Phys. Rev. E* **61**, 2257-2266 (2000).
 49. F. Falo, P. J. Martínez, J. J. Mazo, T. P. Orlando, K. Segall and E. Trías, "Fluxon ratchet potentials in superconducting circuits". *Appl. Phys. A* **75**, 263-269 (2002).
 50. A. J. Sievers and S. Takeno, "Intrinsic localized modes in anharmonic lattices". *Phys. Rev. Lett.* **61**, 970-973 (1988).
 51. S. Takeno and M. Peyrard, "Nonlinear modes in coupled rotator models". *Physica D* **92**, 140-163 (1996).
 52. S. Flach and C. R. Willis, "Discrete breathers". *Phys. Rep.* **295**, 181-264 (1998).
 53. S. Aubry, "Breathers in nonlinear lattices: Existence, linear stability and quantization". *Physica D* **103**, 201-250 (1997).
 54. Focus Issue on "Nonlinear localized modes: Physics and applications". *Chaos* **13(2)** (2003).
 55. E. Trías, J. J. Mazo and T. P. Orlando, "Discrete breathers in nonlinear lattices: experimental detection in a Josephson array". *Phys. Rev. Lett.* **84**,

- 741-744 (2000).
56. P. Binder, D. Abraimov, A. V. Ustinov, S. Flach, and Y. Zolotaryuk, "Observation of breathers in Josephson ladders". *Phys. Rev. Lett.* **84**, 745-748 (2000).
 57. E. Trías, *Vortex motion and dynamical states in Josephson arrays*. Ph.D. thesis, Massachusetts Institute of Technology, 2000.
 58. P. Binder, *Nonlinear localized modes in Josephson ladders*. Ph.D. thesis, Universität Erlangen-Nürnberg, 2001.
 59. M. V. Fistul, "Resonant breather states in Josephson coupled systems". *Chaos*, **13**, 725-732 (2003).
 60. J. J. Mazo, E. Trías and T. P. Orlando, "Discrete breathers in dc-biased Josephson-junction arrays". *Phys. Rev. B* **59**, 13604-13607 (1999).
 61. P. Binder, D. Abraimov and A. V. Ustinov, "Diversity of discrete breathers observed in a Josephson ladder". *Phys. Rev. E* **62**, 2858-2862 (2000).
 62. E. Trías, J. J. Mazo, A. Brinkman and T. P. Orlando, "Discrete breathers in Josephson ladders". *Physica D* **156**, 98-138 (2001).
 63. P. Binder and A. V. Ustinov, "Exploration of a rich variety of breather modes in Josephson ladders". *Phys. Rev. E* **66**, 016603-1(9) (2002).
 64. D. W. Jordan and P. Smith, *Nonlinear ordinary differential equations*. Oxford Univ. Press, 1999.
 65. See the contribution of S. Flach to this book.
 66. A. E. Miroshnichenko, S. Flach, M. V. Fistul, Y. Zolotaryuk and J. B. Page, "Breathers in Josephson junction ladders: Resonances and electromagnetic wave spectroscopy". *Phys. Rev. E* **64**, 066601-1(14) (2001).
 67. M. Schuster, P. Binder and A. V. Ustinov, "Observation of breather resonances in Josephson ladders". *Phys. Rev. E* **65**, 016606-1(6) (2001).
 68. J. J. Mazo, F. Falo and Luis M. Floría, "Josephson-junction ladders: ground state and relaxation phenomena". *Phys. Rev. B* **52**, 10433-10440 (1995).
 69. J. J. Mazo and J. C. Ciria, "Equilibrium properties of a Josephson-junction ladder with screening effects". *Phys. Rev. B* **54**, 16068-16076 (1996).
 70. M. Barahona, S. H. Strogatz and T. P. Orlando, "Superconducting states and depinning transitions of Josephson ladders". *Phys. Rev. B* **57**, 1181-1199 (1998).
 71. E. Trías, J. J. Mazo and T. P. Orlando, "Interactions between Josephson vortices and breathers". *Phys. Rev. B* **65**, 054517-1(10) (2002).
 72. A. Benabdallah, M. V. Fistul and S. Flach, "Breathers in a single plaquette of Josephson junctions: existence, stability and resonances". *Physica D* **159**, 202-214 (2001).
 73. M. V. Fistul, S. Flach and A. Benabdallah, "Magnetic-field-induced control of breather dynamics in a single plaquette of Josephson junctions". *Phys. Rev. E* **65**, 046616-1(4) (2002).
 74. F. Pignatelli and A. V. Ustinov, "Observation of breather-like states in a single Josephson cell". *Phys. Rev. E* **67**, 036607-1(7) (2003).
 75. J. J. Mazo, "Discrete breathers in two-dimensional Josephson-junction arrays", *Phys. Rev. Lett.* **89**, 234101-1(4) (2002).
 76. D. Zueco and J. J. Mazo, private communication.